Flotillin-upregulation acts as an epithelial-mesenchymal transition driver by promoting sphingosine kinase 2-dependent AXL stabilization

Running title : Upregulated-flotillins drive EMT via SphK2 and AXL

Mallory Genest[1], Franck Comunale[1], Eduardo Rios-Morris[1], Damien Planchon[1], Pauline Govindin[1], Sophie Vacher[2], Ivan Bièche[2], Bruno Robert[3], Himanshu Malhotra[1], Andreas Schoënit[1], Liubov A. Tashireva[4], Cécile Gauthier-Rouvière[1#] and Stéphane Bodin[1#]

[1] *CRBM, University of Montpellier, CNRS,* 1919 route de Mende, 34293 *Montpellier, France,*

[2] Department of Genetics, Institut Curie, Paris, France.

[3] IRCM, Campus Val d'Aurelle, 208 avenue des Apothicaires, 34298 Montpellier, France

[4] Cancer Research Institute, Tomsk National Research Medical Center, Russian Academy of Sciences, Tomsk, Russia

[#]Authors equally contributed to this work

Abstract

Epithelial-to-mesenchymal transition (EMT) is critical for cancer cell dissemination and metastasis formation. Here, we found that flotillin 1 and 2 upregulation, which is observed in many aggressive cancers, is sufficient to induce EMT in non-tumoral mammary cells. We identified that the Upregulated Flotillin-Induced Trafficking (UFIT) pathway promotes the endocytosis of several transmembrane receptors in flotillin-positive late endosomes, thus modifying their destiny and leading to the the activation of oncogenic pathways that promotes EMT. The receptor tyrosine kinase AXL, a key actor during EMT and metastasis formation, is stabilized by the UFIT pathway and is required for EMT induced by flotillin upregulation. Moreover, sphingosine kinase 2, a lipid kinase recruited in flotillin-positive plasma membrane domains and vesicles, is required to stabilize AXL.

These findings show that flotillin upregulation is a key EMT inducer. The UFIT pathway, through sphingosine kinase 2 activity, targets membrane receptors, such as AXL, to flotillin-positive vesicles, allowing their stabilization and the activation of EMT-linked signaling pathways.

Introduction

Cancer progression is a multistep process involving both genetic and epigenetic changes that independently or in cooperation generate metastatic tumors. One key step in this process is the aberrant reactivation of epithelial-to-mesenchymal (EMT) transition, an essential embryonic process that is, crucial for tumor initiation and cancer cell dissemination during metastatic progression (review in (*1*)). EMT induction is orchestrated by a family of EMT-inducing transcription factors (such as ZEB1/2, Snail1, Slug) that are regulated by multiple signaling pathways known to play a role during embryogenesis and also tumor development [e.g. TGFβ receptors, Receptor Tyrosine Kinases (RTKs) and the downstream signaling pathways Ras/MAPK and PI3-K/AKT, WNT, NOTCH] (*2*). These oncogenic signaling pathways are considered cancer drivers, and some of them are used as biomarkers for currently used targeted therapies, while others are potential biomarkers for therapies still under development. Because of EMT pleiotropic roles in the acquisition of invasive properties and of therapeutic resistance, it is important to identify new inducers of this cellular program. For instance, the RTK AXL is an attractive candidate target for anticancer therapies (review in (*3*)). AXL expression is low in normal adult tissues, but is overexpressed in several tumors, and this is associated with shorter overall survival. Aberrant AXL expression is associated with EMT, invasion, metastasis formation, cell proliferation, tumor angiogenesis, reduced anti-cancer immune response, stem cell maintenance, and treatment resistance in many tumor types (*4*, *5*). AXL is a member of the TAM (Tyro3, AXL, Mer) family of RTK that is activated through several mechanisms, including binding to its ligand Gas6, homodimerization in condition of overexpression, and crosstalk with other RTKs (review in (*4*)). However, AXL genetic mutations and amplification events are rare, despite its upregulation in many tumor types, supporting the role of post-transcriptional/translational regulation of AXL expression.

The endosomal system is known to accumulate activated receptors and signaling molecules. It is now clear that endocytosis, whereas considered for many years as only a mean of limiting signal transduction, is crucial to maintain and even generate signaling pathways (*6–8*).

Flotillin 1 and 2 are two ubiquitous and highly conserved homologous proteins. Their upregulation in a subset of all solid tumors has been associated with poor patient prognosis and high risk of metastasis formation (*9–12*). When co-upregulated, flotillins promote plasma membrane (PM) invaginations and favor an endocytic pathway we named Upregulated Flotillins-Induced trafficking (UFIT) pathway (*13–15*). This UFIT pathway targets protein cargos to non-degradative late endosomes in which flotillins accumulate (*16–19*). Several independent studies performed in cancer cell lines reported that flotillins influence the activation of signaling pathways promoting EMT and cellular invasion and that they are scaffolding factors for several signaling molecules (*20*). Therefore, the UFIT pathway, at the crossroad between endocytosis and signaling, emerges as an interesting mechanism in the regulation of oncogenic pathways. To study the contribution of flotillin-induced deregulation of the endosomal system to EMT, we reproduced the flotillin 1 and 2 co-upregulation observed in tumors in non-tumoral mammary cell lines (MCF10A and NMuMG) that naturally display low flotillin expression level. Indeed, all previous studies on flotillin role in EMT and cell invasion (*10*, *11*) were carried out in cancer cell lines harboring several mutations in signaling and structural genes that promote EMT induction and invasion. This did not allow determining the exact contribution of flotillin upregulation and limited the characterization of the molecular mechanisms specifically deregulated upon flotillin upregulation. In non-tumoral cells, we found that flotillin upregulation is sufficient to promote EMT and to activate key oncogenic signaling pathways. We also observed that in zebrafish embryos, flotillin 2 is enriched in neural crest cells (NCC), where EMT occurs physiologically, and that defective flotillin expression impairs NCC migration and formation of NCC-derived tissues. In MCF10A cells, we identified AXL

as a major contributor to EMT induced by flotillin upregulation. Using optogenetics to force flotillin oligomerization at the PM in living cells, we demonstrated that AXL is trapped in flotillin microdomains. We then found that the UFIT pathway promotes i) AXL endocytosis towards flotillin-positive late endosomes bearing the characteristics of signaling endosomes that contain activated PM receptors and also K-Ras4B; and ii) AXL stabilization, leading to its overexpression. In non-tumoral cell lines in which flotillins are upregulated and also in invasive MDA-MB-231 breast cancer cells where flotillins are endogenously overexpressed, AXL stabilization by the UFIT pathway depends on the lipid kinase sphingosine kinase 2 (SphK2) that produces the bioactive lipid sphingosine 1-phosphate (S1P), a key signaling component of the sphingolipid metabolic network during tumorigenesis.

Results

Flotillin upregulation in non-tumoral mammary epithelial cells is sufficient to induce EMT

To precisely determine the role of flotillin upregulation in EMT and the molecular mechanisms that are deregulated upon flotillin upregulation, we used non-tumoral epithelial cell lines (human MCF10A and murine NMuMG) in which oncogenic pathways are not activated and with low endogenous flotillin expression levels. From these two cell lines, we generated stable cell lines (MFC10AF1F2 and NMuMGF1F2) that express flotillins at levels similar to those observed in MDA-MB-231 invasive breast cancer cells (Fig. S1 A-C and (*16*)).

First, to identify the gene expression changes and the downstream signaling pathways associated with flotillin upregulation, we compared by RNA-sequencing (RNA-seq) the expression profiles of control MCF10AmCh cells (transfected with the empty mCherry vector, mCh) and MCF10AF1F2 cells (transfected with flotillin 1-HA and flotillin 2-mCherry). By using two differential gene expression analysis pipelines (Tuxedo and DSeq2), we identified 232 upregulated and 570 downregulated genes (802 genes in total, fold change 2.8, $P<0.05$) in MCF10AF1F2 cells compared with control cells (Table S1). Gene ontology (GO) cluster analysis (Fig. 1 A) to determine the function of these 802 genes revealed that flotillin upregulation was associated with deregulation of genes involved in extracellular matrix, cell adhesion, migration, differentiation, apoptosis and signaling pathways, particularly MAP kinases. These processes are often deregulated during tumor development and particularly during EMT.

To confirm that flotillin upregulation was associated with differential expression of EMT-specific genes, we compared the list of genes differentially expressed between MCF10AmCh and MCF10AF1F2 cells with the EMT transcriptional signature previously established by a meta-analysis that combined 18 independent gene expression studies on EMT induced by

different treatments in different cell types (*21*). One third (22/67) of the upregulated genes and more than half (39/62) of the downregulated genes in this EMT signature overlapped with the genes that were deregulated upon flotillin overexpression in MCF10A cells (Fig. 1 B). Particularly, analysis of the top 20 up- and down-regulated genes highlighted the decreased expression of E-cadherin and occludin, concomitantly with the increased expression of ZEB1, fibronectin, vimentin and N-cadherin (Fig. 1 C).

We validated these results in MCF10AF1F2 and NMuMGF1F2 cells by RT-qPCR (Fig. 1 D and S1 D), western blot and immunocytochemistry analysis (Fig. 1 E-G and S1 E-G). We confirmed the downregulation (mRNA and protein) of the hallmark epithelial marker E-cadherin (Fig. 1 D-F and S1 D-F) and of the polarity marker ZO-1 (Fig. 1 G and S1 G), and the upregulation of the mesenchymal markers N-cadherin and vimentin (Fig. 1 D-G and S1 D-F). Morphological analysis using scanning electron microscopy and F-actin cytoskeleton staining showed that cell polarity was lost in NMuMGF1F2 cells (flotillin upregulation) compared with NMuMGmCh cells (transfected with the empty mCherry vector) (Fig. 1 H-I).

In conclusion, flotillin upregulation in non-tumoral mammary epithelial cells is sufficient to induce EMT.

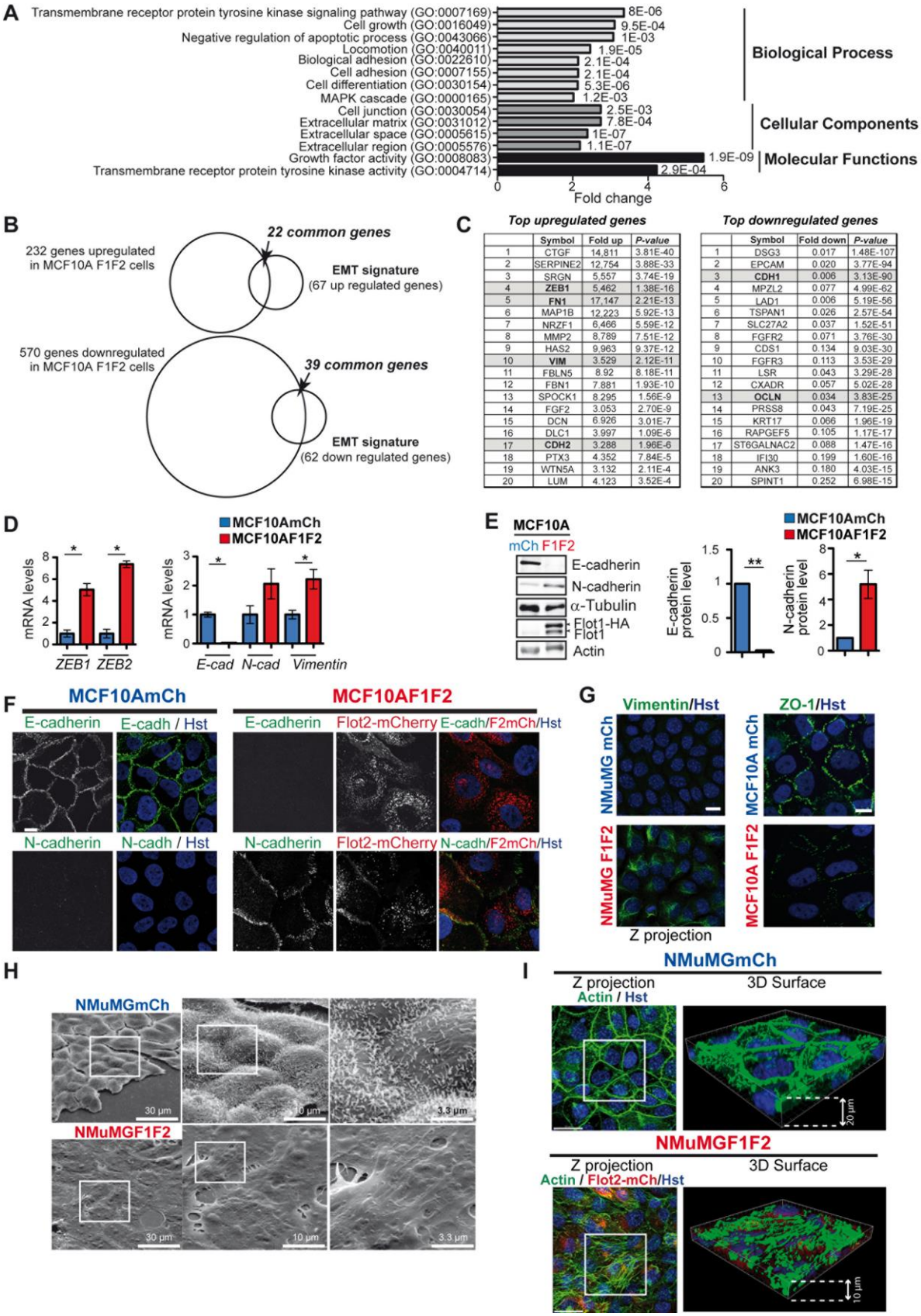

Top upregulated genes

	Symbol	Fold up	*P-value*
1	CTGF	14,811	3.81E-40
2	SERPINE2	12,754	3.88E-33
3	SRGN	5,557	3.74E-19
4	**ZEB1**	5,462	1.38E-16
5	**FN1**	17,147	2.21E-13
6	MAP1B	12,223	5.92E-13
7	NRZF1	6,466	5.59E-12
8	MMP2	8,789	7.51E-12
9	HAS2	9,963	9.37E-12
10	**VIM**	3.529	2.12E-11
11	FBLN5	8.92	8.18E-11
12	FBN1	7.881	1.93E-10
13	SPOCK1	8.295	1.56E-9
14	FGF2	3.053	2.70E-9
15	DCN	6.926	3.01E-7
16	DLC1	3.997	1.09E-6
17	**CDH2**	3.288	1.96E-6
18	PTX3	4.352	7.84E-5
19	WTN5A	3.132	2.11E-4
20	LUM	4.123	3.52E-4

Top downregulated genes

	Symbol	Fold down	*P-value*
1	DSG3	0.017	1.48E-107
2	EPCAM	0.020	3.77E-94
3	**CDH1**	0.006	3.13E-90
4	MPZL2	0.077	4.99E-62
5	LAD1	0.006	5.19E-56
6	TSPAN1	0.026	2.57E-54
7	SLC27A2	0.037	1.52E-51
8	FGFR2	0.071	3.76E-30
9	CDS1	0.134	9.03E-30
10	FGFR3	0.113	3.53E-29
11	LSR	0.043	3.29E-28
12	CXADR	0.057	5.02E-28
13	**OCLN**	0.034	3.83E-25
14	PRSS8	0.043	7.19E-25
15	KRT17	0.066	1.96E-19
16	RAPGEF5	0.105	1.17E-17
17	ST6GALNAC2	0.088	1.47E-16
18	IFI30	0.199	1.60E-16
19	ANK3	0.180	4.03E-15
20	SPINT1	0.252	6.98E-15

Figure 1

Figure 1: Flotillin upregulation in non-tumoral epithelial mammary MCF10A cells induces EMT.
A) GO identification of the biological process, cellular component and molecular function terms associated with the 802 genes that were differentially expressed in MCF10AF1F2 cells compared with MCF10AmCh cells.
B) Venn diagrams comparing the genes that we found to be up- or down-regulated (> or <2.8, $p<0.05$) by RNA-seq data analysis in MCF10AF1F2 *versus* MCF10AmCh cells with the EMT signature established by (*21*).
C) Top 20 up- and down-regulated genes in MCF10AF1F2 cells that were retrieved from the EMT signature. P values were adjusted for multiple testing using the Benjamini-Hochberg procedure.
D) RT-qPCR analysis of the mRNA levels of ZEB1, ZEB2, E-cadherin, vimentin and N-cadherin in MCF10AmCh and MCF10AF1F2 cells. Data are the mean ± SEM of four independent experiments. *P<0.05.
E) Western blot analysis of whole MCF10AmCh and MCF10AF1F2 cell lysates to investigate the expression of E- and N-cadherin, tubulin and flotillin 1. Data are the mean ± SEM of at least four independent experiments. *P<0.05; **P<0.01.
F, G) Confocal images showing the distribution of E- and N-cadherin, flotillin 2-mCherry and ZO-1 in MCF10AmCh and MCF10AF1F2 cells and of vimentin in NMuMGmCh and NMuMGF1F2 cells, analyzed by immunocytochemistry. Nuclei were stained with Hoechst (Hst; blue). In G, for vimentin staining, the z projection corresponds to the stacked signal of 30 plans performed every 0.3 µm. Images are representative of 3 independent experiments. Scale bar: 10 µm.
H) Scanning electron microscopy images of the monolayer formed by NMuMGmCh and NMuMGF1F2 cells.
I) Z-projection and 3D surface reconstruction of NMuMGmCh and NMuMGF1F2 cells after staining for F-actin, flotillin 2-mCherry and Hoechst (nuclei), performed with 35 plans for NMuMGmCh and 22 plans for NMuMGF1F2 every 0.3.µm. Images are representative of 3 independent experiments. Scale bar: 10 µm

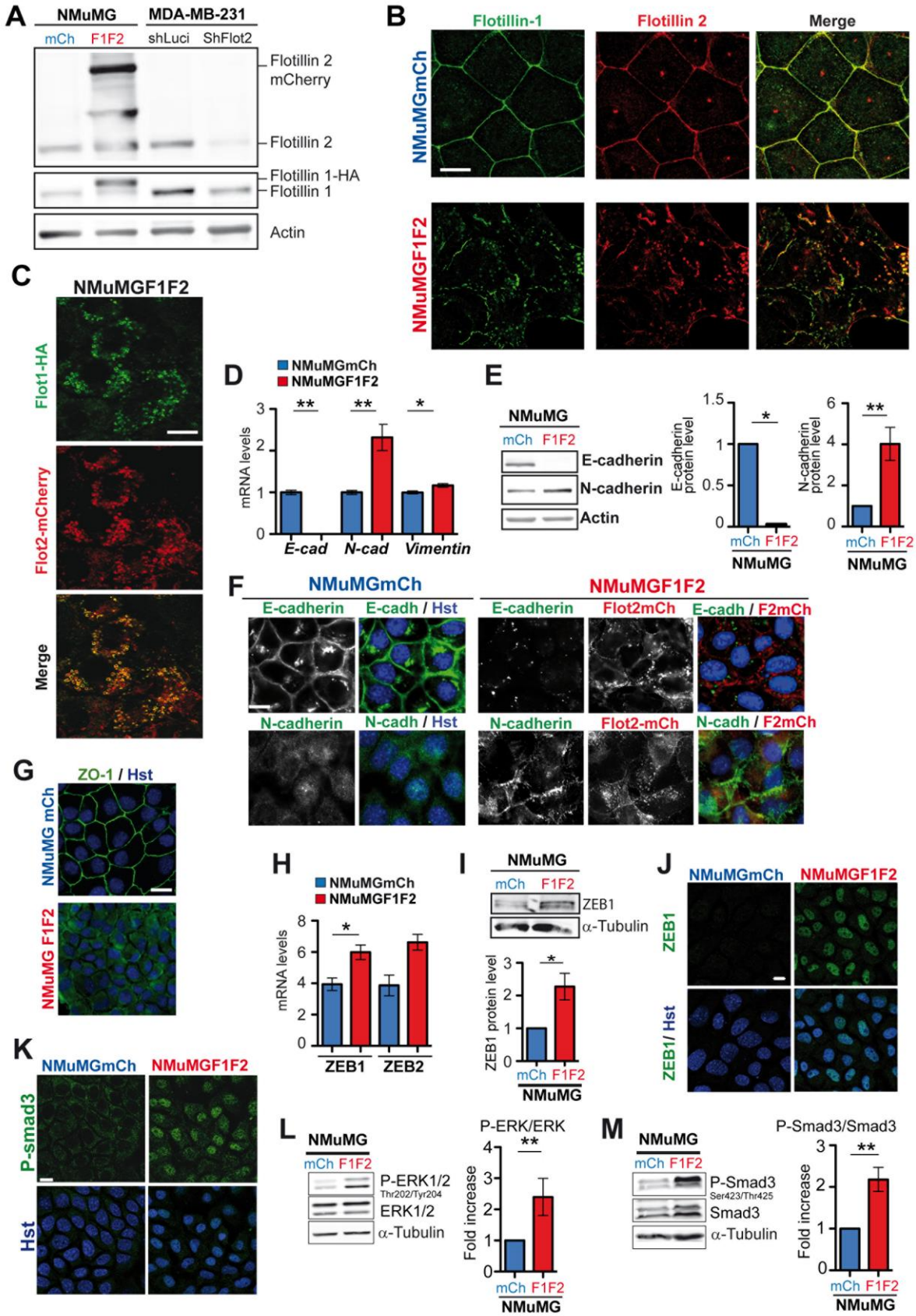
A
NMuMG
MDA-MB-231
mCh
F1F2
shLuci
ShFlot2
Flotillin 2 mCherry
Flotillin 2
Flotillin 1-HA
Flotillin 1
Actin
B
Flotillin-1
Flotillin 2
Merge
NMuMGmCh
NMuMGF1F2
C
NMuMGF1F2
Flot1-HA
Flot2-mCherry
Merge
D
NMuMGmCh
NMuMGF1F2
mRNA levels
E-cad
N-cad
Vimentin
E
NMuMG
E-cadherin
N-cadherin
Actin
E-cadherin protein level
N-cadherin protein level
F
NMuMGmCh
NMuMGF1F2
E-cadherin
E-cadh / Hst
Flot2mCh
E-cadh / F2mCh
N-cadherin
N-cadh / Hst
Flot2-mCh
N-cadh / F2mCh
G
ZO-1 / Hst
NMuMG mCh
NMuMG F1F2
H
NMuMGmCh
NMuMGF1F2
mRNA levels
ZEB1
ZEB2
I
NMuMG
ZEB1
α-Tubulin
ZEB1 protein level
J
NMuMGmCh
NMuMGF1F2
ZEB1
ZEB1/ Hst
K
NMuMGmCh
NMuMGF1F2
P-smad3
Hst
L
NMuMG
P-ERK1/2
Thr202/Tyr204
ERK1/2
α-Tubulin
P-ERK/ERK
Fold increase
M
NMuMG
P-Smad3
Ser423/Thr425
Smad3
α-Tubulin
P-Smad3/Smad3
Fold increase

FigureS1

Figure S1: Flotillin upregulation induces EMT in the NMuMG non-tumoral murine epithelial mammary cell line.

A) Lysates of NMuMG cells that stably express mCherry (NMuMGmCh) or both flotillin 1-HA and flotillin 2-mCherry (NMuMGF1F2) were analyzed by western blotting using antibodies against flotillin 1 and flotillin 2. In NMuMGF1F2 cells, flotillin levels were comparable to the ones detected in the invasive mammary tumor MDA-MB-231 cell line. Lysates from MDA-MB-231shFlot2 cells (generated using a shRNA against *FLOT2* to knockdown both flotillins (*16*)) also were analyzed. Actin was used as loading control.

B) Confocal images showing that endogenous flotillin 1 and 2 are localized at the plasma membrane in NMuMGmCh cells, whereas they translocate to vesicular compartments, where they co-localize, in NMuMGF1F2 cells, as previously shown in MCF10AF1F2 and in MDA-MB-231 cells (*16*).

C) Confocal images showing the co-localization of flotillin 1-HA and flotillin 2-mCherry in intracellular vesicles in NMUMGF1F2 cells. Scale bar: 10 µm.

D, H) RT-qPCR analysis of the mRNA levels of E-cadherin, N-cadherin and vimentin (D) and of ZEB1 and ZEB2 (H) in NMuMGmCh and NMuMGF1F2 cells. Histograms show the mean ± SEM of 4 independent experiments. *P<0.05; **P<0.01.

E, I) Western blotting performed using cell lysates from NMuMGmCh and NMuMGF1F2 cells to compare the amount of E- and N-cadherin (E), and ZEB1 (I). Histograms show the mean ± SEM of at least 4 independent experiments. *P<0.05; **P<0.01.

F, G) Comparison of the distribution of endogenous E-, N-cadherin (F) and ZO-1 (G) in NMuMGmCh and NMuMGF1F2 cells analyzed by immunofluorescence. Nuclei are stained with Hoechst (Hst, blue). Images are representative of 3 independent experiments.

J) Confocal images of ZEB1 localization and nuclei stained with Hoechst (Hst, blue) in NMuMGmCh and NMuMGF1F2 cells.

L, M) Cell lysates from NMuMGmCh and NMuMGF1F2 cells were analyzed by western blotting to evaluate the phosphorylation status of ERK1/2 (L) and Smad3 (M). Histograms (mean ± SEM of 4 independent experiments) show the quantification of the phospho-signal normalized to the total amount of each protein. **P<0.01.

K) NMuMGmCh and NMuMGF1F2 cells were labeled with a anti-Smad3 phosphorylated on S423/425 antibody and with Hoechst (Hst).

Scale bars in B, C, F, G, J and K: 10µm.

In zebrafish embryos, flotillin 2 is upregulated in neural crest cells undergoing EMT and is required for their migration.

To examine *in vivo* flotillin contribution to the EMT process, we took advantage of the zebrafish embryo model in which NCC undergo EMT and migration during early development (*22*). To visualize NCC, we used *foxd3:GFP* zebrafish transgenic embryos that express GFP under the control of the foxd3 promoter. In 18-hour post-fertilization (hpf) embryos, flotillin 2 was strongly expressed in migrating NCC at the dorsal side of the neural tube compared with the surrounding cells (Fig. S2 A). Then, using a specific anti-sense morpholino oligonucleotide we knocked-down flotillin 2 (MoFlot2 embryos). This led to a reduction also of flotillin 1

expression, as previously reported (*23*). We showed that NCC migration (Fig. S2 B-E) and the formation of NCC-derived tissues, such as jaws and branchial arches (Fig. S2 E), were strongly altered in MoFlot2 embryos compared with control embryos (MoCTL; control morpholino).

This data suggest that flotillin upregulation plays a key role in EMT not only in the context of tumor cell invasion, but also during embryonic development.

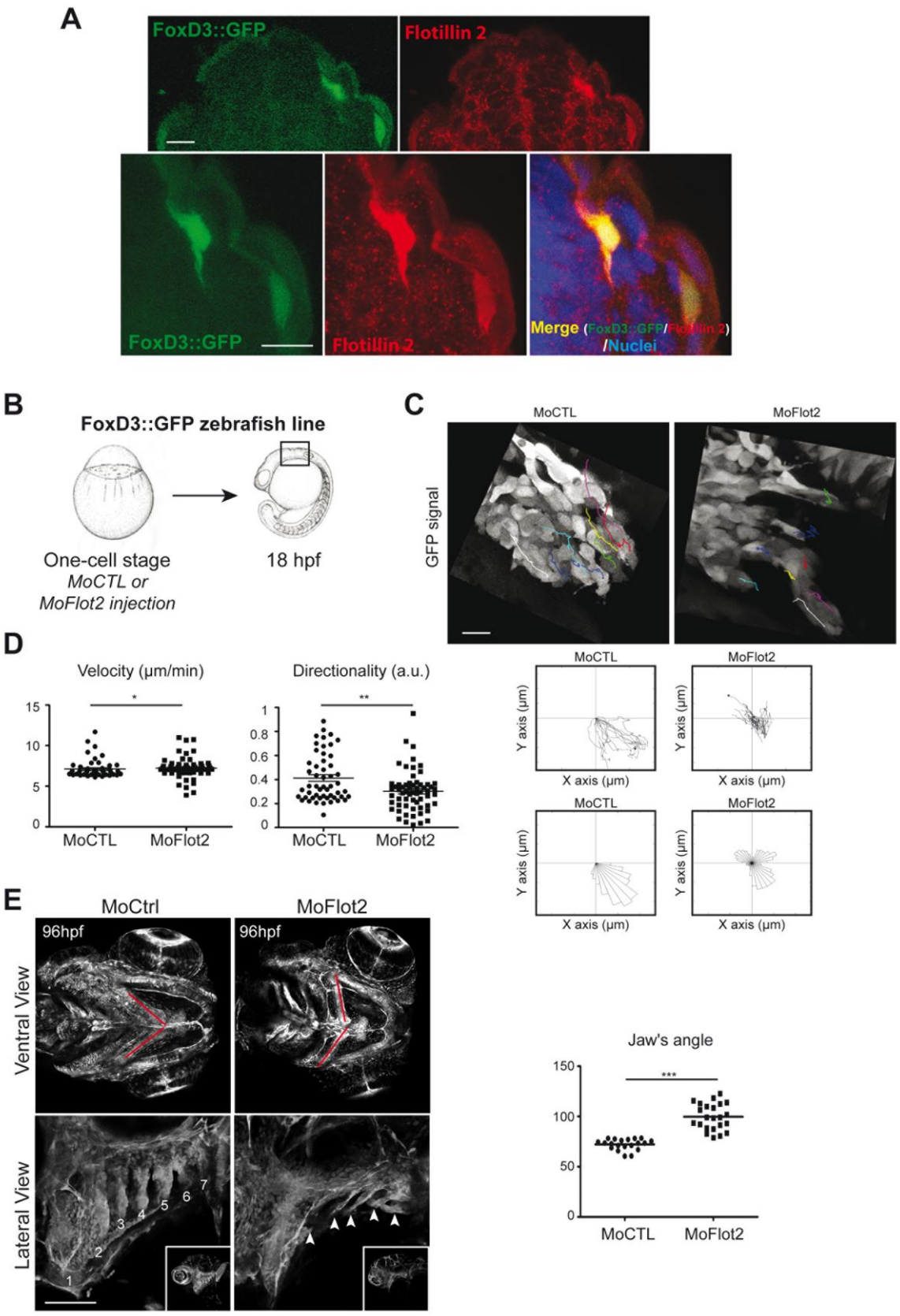
A
FoxD3::GFP
Flotillin 2
FoxD3::GFP
Flotillin 2
Merge (FoxD3::GFP/Flotillin 2)
/Nuclei
B
FoxD3::GFP zebrafish line
One-cell stage
MoCTL or
MoFlot2 injection
18 hpf
C
MoCTL
MoFlot2
GFP signal
MoCTL
MoFlot2
Y axis (µm)
X axis (µm)
D
Velocity (µm/min)
Directionality (a.u.)
MoCTL
MoFlot2
E
MoCtrl
MoFlot2
96hpf
96hpf
Ventral View
Lateral View
Jaw's angle
MoCTL
MoFlot2

Figure S2

Figure S2. Flotillin 2 is upregulated *in vivo* in neural crest cells (NCC) undergoing EMT in zebrafish embryos, and is required for their migration and the formation of NCC tissue derivatives.

A) *Endogenous flotillin expression in neural crest cells.* Representative confocal images of endogenous flotillin 2 overexpression (red) in migrating cranial NCC (green) in Tg(*foxd3:GFP*) embryos at 18hpf. Scale bar: 10µm.

B-D) *Flotillin2 is necessary for neural crest migration.* B: Control (MoCTL) or flotillin 2 morpholinos (MoFlot2) were injected in Tg(*foxd3:GFP*) embryos at the 1-cell stage. At 18hpf, embryos were mounted for time-lapse microscopy to analyze NCC migration. (C): Representative images of NCC in control (MoCTL) and MoFlot2 embryos. Some NCCs are colored to follow their movement during the recording period. Scale bar: 20µm. Representative NCC trajectories in the X or Y axis during 2 hours. (D) Boxplots showing the quantification of the velocity and persistence of migration in 8hpf control (MoCTL) and MoFlot2 embryos for 2 hours. At least 15 embryos were analyzed, and 50 cells were tracked for each condition. The values of velocity and persistence are the mean $\pm$ SEM of 3 independent experiments, * $p < 0.05$, ** $p < 0.01$ (unpaired Student's *t* test).

E) *Flotillin downregulation affects formation of neural crest tissue derivatives.* The developing cartilage of the branchial arches and jaws, tissue derivatives of NCC, were analyzed in 96hpf Tg(*Fli1:GFP*) control (MoCTL) and MoFlot2 embryos. MoFlot2 larvae observed from the ventral side presented a jaw angle that reflects a defects in NCC migration compared with control animals. Lateral side observation identified the impaired formation of branchial arches in MoFlot2 embryos (arrows) compared with control where these structures are formed. The measure of the jaw angle confirmed the defect in MoFlot2 embryos. Scale bar: 20µm. At least 20 larvae were analyzed and the angle values are the mean $\pm$ SEM of 3 independent experiments, *** $p < 0.0001$, unpaired Student's *t* test.

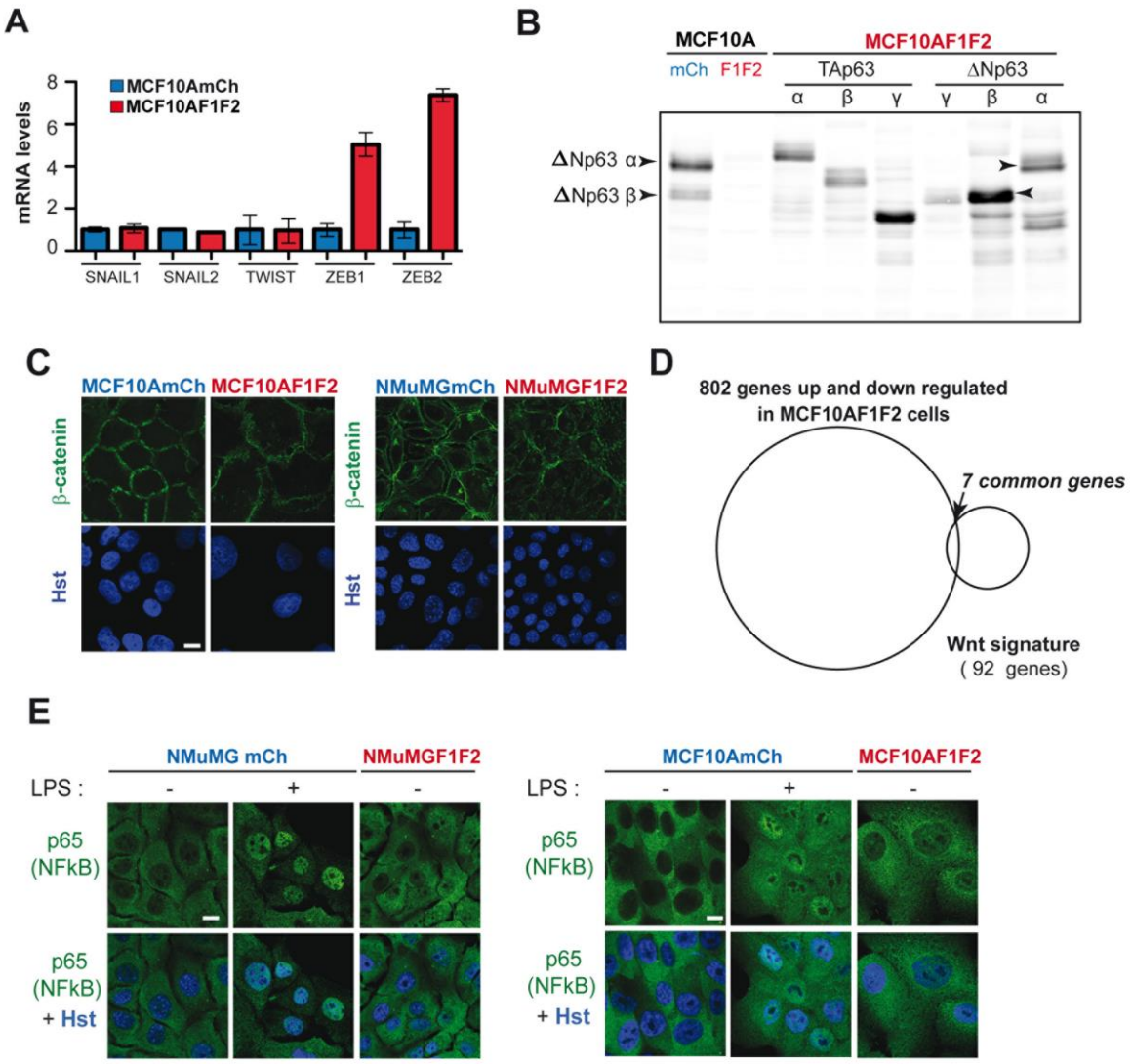

Figure S3: Identification of non-activated signaling pathways downstream of flotillin upregulation in mammary epithelial cells and determination of the p63 isoforms expressed in MCF10AmCh cells and downregulated in MCF10AF1F2 cells.

A) *Characterization of the transcriptional repressors of E-cadherin expression*. RT-qPCR analysis of the mRNA levels of Snail1, Snail2, Twist, ZEB1, ZEB2 in MCF10AmCh and MCF10AF1F2 cells. Histograms show the mean ± SEM of 3 independent experiments.

B) *Characterization of the p63 isoforms expressed in MCF10AmCh and MCF10AF1F2 cells.* Western blot analysis of the p63 isoforms in cell lysates from MCF10AmCh, MCF10AF1F2 cells and MCF10AF1F2 cells transfected with the different non-tagged p63 isoforms (TAp63α, β, γ or ΔNp63α, β, γ) using an antibody against all p63 isoforms. ΔNp63α and to a lesser extent ΔNp63β are the two mains isoforms expressed in MCF10A cells. The expression of ΔNp63α and of ΔNp63β was abolished in MCF10AF1F2 cells.

C, D, E) *The oncogenic NF-kB and WNT canonical signaling pathways are not activated following flotillin upregulation in MCF10A and NMuMG cells.* **C)** β-catenin distribution analyzed by immunofluorescence is similar in MCF10AmCh and MCF10AF1F2 cells and NMuMGmCh and NMuMGF1F2 cells, and no nuclear staining was detected, indicating that the WNT canonical pathway is not activated. Nuclei are stained with Hoechst (Hst). Scale bar: 10 µm. **D)** Venn diagrams illustrating the small overlap between the 802 differentially expressed genes identified by RNA-seq in MCF10AF1F2 cells *versus* MCF10AmCh cells and the 92 differentially expressed genes identified in an established WNT signature. Only 7/92 genes overlapped. **E)** Cellular distribution of the NF-kB p65

subunit, analyzed by immunofluorescence, in MCF10AmCh and MCF10AF1F2 cells and in NMuMGmCh and NMuMGF1F2 cells. In all cases, NF-kB p65 was excluded from the nucleus, indicating that the NF-kB pathway is not activated upon flotillin upregulation. As positive control, MCF10AmCh cells and NMuMGmCh cells were stimulated with lipopolysaccharide LPS (1µg/ml, 1h) to induce NF-kB p65 translocation to the nucleus. Scale bar: 10 µm.

Flotillin upregulation mediates E-cadherin loss through ΔNP63/ZEB transcription factors

We then focused on the mechanisms by which upregulated flotillins promote E-cadherin downregulation, one of the EMT hallmarks. Several transcription factors, such as Snail1, Snail2, Twist, ZEB1 and ZEB2, can inhibit E-cadherin expression (*24*). Flotillin upregulation did not affect Snail 1/2 and Twist expression, as shown by the transcriptomic analysis and by quantification of their mRNA levels (Fig. S3 A). Conversely, it induced ZEB 1 and 2 mRNA expression (Fig. 2 A and Fig. S1 H) and ZEB1 protein expression (Fig. 2 B and Fig. S1 I) (no anti-ZEB2 antibody is available). ZEB1 localized in the nucleus (Fig. 2 C and S1 J). Moreover, ZEB1/2 knockdown in MCF10AF1F2 cells restored E-cadherin expression (Fig. 2 B) and its accumulation at cell-cell contacts (Fig. 2 D). This demonstrated the key role of ZEB1/2 in E-cadherin downregulation upon flotillin upregulation.

In MCF10A cells, expression of hyperactive H-Ras mutant or its downstream effector PI3-K leads to ZEB1/2-dependent E-cadherin downregulation and EMT *via* the transcriptional repression of ΔNp63α, the predominant p63 isoform in MCF10A cells (*25*). ΔNp63α downregulation is an EMT marker in these cells (*25*, *26*). Flotillin upregulation in MCF10A cells led to reduction of ΔNp63α and ΔNp63β expression (western blotting and immunocytochemistry, Fig. 2 E-F and S 3B; and Table S1). We excluded ZEB 1 and 2 implication in ΔNp63α downregulation through a negative feed-back loop because ZEB1 and 2 knock-down did not rescue ΔNp63α expression in MCF10AF1F2 cells (Fig. 2 F). Moreover, data obtained from a cohort of 527 patients with breast cancer indicated that flotillin 1 and ΔNp63 mRNA expression levels were negatively correlated (Fig. 2 G).

In conclusion, our data indicate that flotillin upregulation promotes the decrease of ΔNp63α expression, allowing the expression of ZEB1 and 2 that repress E-cadherin expression, thus contributing to EMT.

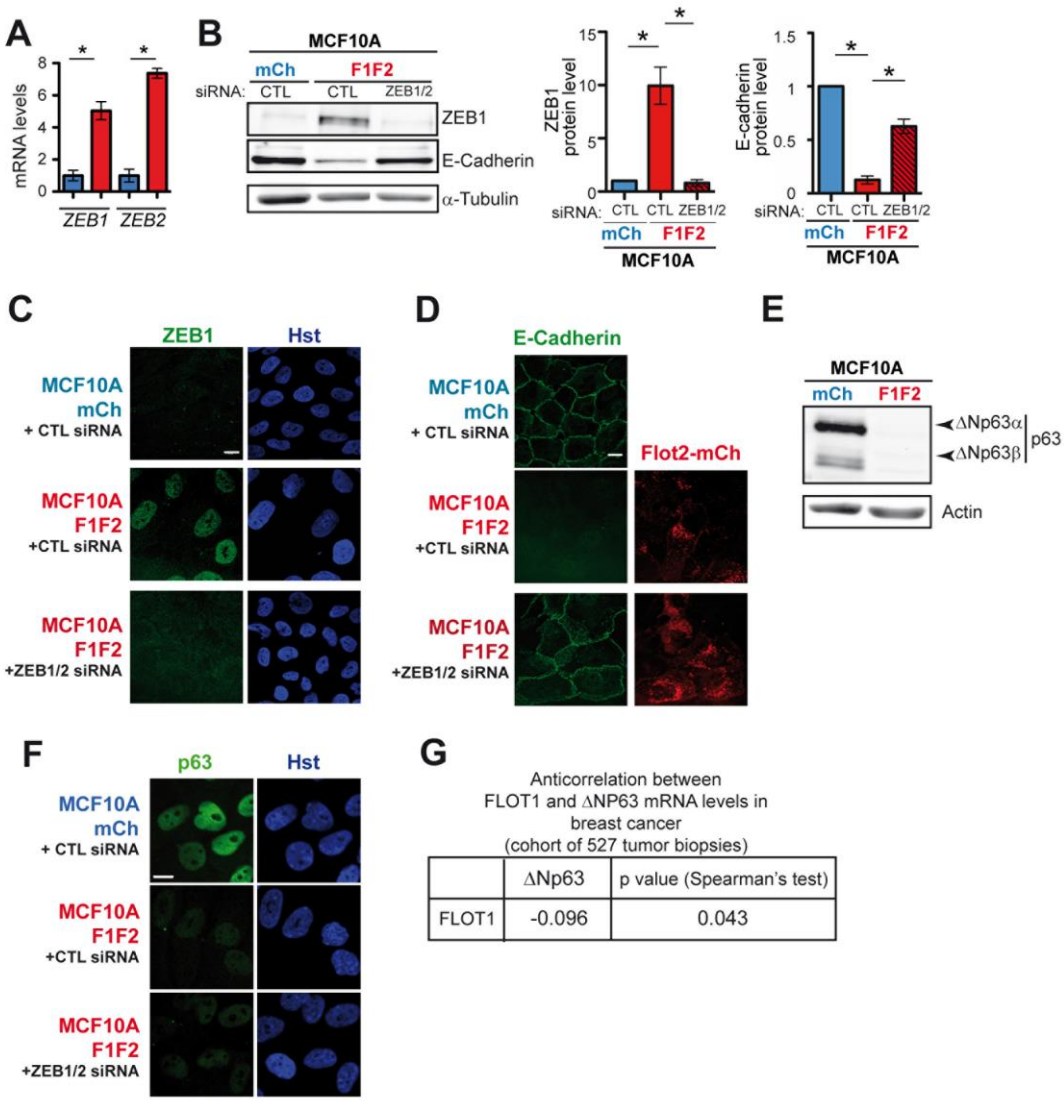

Figure 2: Flotillin upregulation induces the loss of E-cadherin in a ΔNP63α/ZEB- dependent manner

A) RT-qPCR analysis of the mRNA levels of ZEB1 and ZEB2 in MCF10AmCh and MCF10AF1F2 cells. Data are the mean ± SEM of four independent experiments. *P<0.05.

B) Western blotting to assess ZEB1, E-cadherin and α-tubulin expression in cell lysates from MCF10AmCh cells and MCF10AF1F2 cells transfected with siRNAs against ZEB1/2 or control siRNA (CTL). Histograms (mean ± SEM of 4 independent experiments) show the quantification of the amount of each protein in the indicated conditions.

C, D and F) Distribution of ZEB1 (C), E-cadherin (D), and p63 (F) in MCF10AmCh cells and and in ZEB1/2 siRNA- or CTL siRNA-transfected MCF10AF1F2 cells analyzed by immunofluorescence using specific antibodies. In C and F, nuclei were stained with Hoechst (Hst). Scale bars: 10 µm.

E) ΔNp63α and β expression in MCF10AmCh and MCF10AF1F2 cells analyzed by western blotting using an antibody against all p63 isoforms. Characterization of the p63 isoforms allowed identifying ΔNp63α and β as the isoforms mainly expressed in MCF10AmCh cells (Fig. S2 B).
G) Analysis of the correlation between the mRNA levels of *FLOT1* and p63 in breast cancer biopsies from 527 patients.
*P<0.05; **P<0.01; ***P<0.001

Flotillin upregulation in non-tumoral mammary epithelial cells is sufficient to activate several oncogenic signaling pathways

The GO analysis of the genes that were differentially expressed between control and flotillin-upregulated MCF10A cells revealed a strong association with signal transduction pathways, particularly those involving transmembrane RTKs and the MAPK pathway (Fig. 1 A). Different bioinformatics analysis [DAVID, Enrich R analysis of the Kyoto Encyclopedia of Genes and Genomes (KEGG) pathways, and Genomatix] identified the PI3-K/AKT pathway and the Ras pathway, two major oncogenic signaling pathways (Table S2). In agreement, analysis of the phosphorylation profile of some kinases and of their protein substrates using the human Phospho-kinase Array revealed the increased phosphorylation of at least four main tyrosine (Y) and serine/threonine (S/T) kinases involved in oncogenic signaling pathways (ERK1/2, FAK, AKT, Fyn) and of their substrates (Hsp27, STAT) (Fig. 3 A). These data confirmed that flotillin upregulation in cells without oncogenic mutations (MCF10A and NMuMG cells) increases the activity of major oncogenic pathways. We demonstrated activation (Fig. 3 B) in MCF10AF1F2 cells compared with MCF10AmCh cells, as well as ERK and PI3-K/AKT activation, as indicated by the increased phosphorylation of ERK1/2 at T202/Y204 (Fig. 3 C, S1 L), the increased nuclear localization of ERK2-GFP (Fig. 3D), and the increased phosphorylation of AKT at S473 of STAT3 at Y705(Fig. 3 E-F) in MCF10AF1F2 cells.

High TGF-β signaling pathway activity contributes to tumor development, notably through its ability to induce EMT (*1*), and flotillins were reported to participate in the activation of this pathway in nasopharyngeal carcinoma (*10*, *11*). Here, we found that flotillin upregulation in

non-tumoral cells also activated the TGF-β signaling pathway, as indicated by the significantly higher Smad3 phosphorylation at S423/T425 (Fig. 3 G and S1 M) and the nuclear localization of phosphorylated Smad3 (Fig. 3 H and S1 K) in MCF10AF1F2 and NMuMGF1F2 cells compared with control cells (mCh).

Although several oncogenic pathways were activated upon flotillin upregulation, we never detected activation of the NF-kB and WNT canonical pathways (Fig. S3 C-E).

Altogether, these data demonstrated that flotillin upregulation in non-tumoral cells is sufficient to activate the key oncogenic Ras/ERK MAP kinase, AKT and TGF-β signaling pathways.

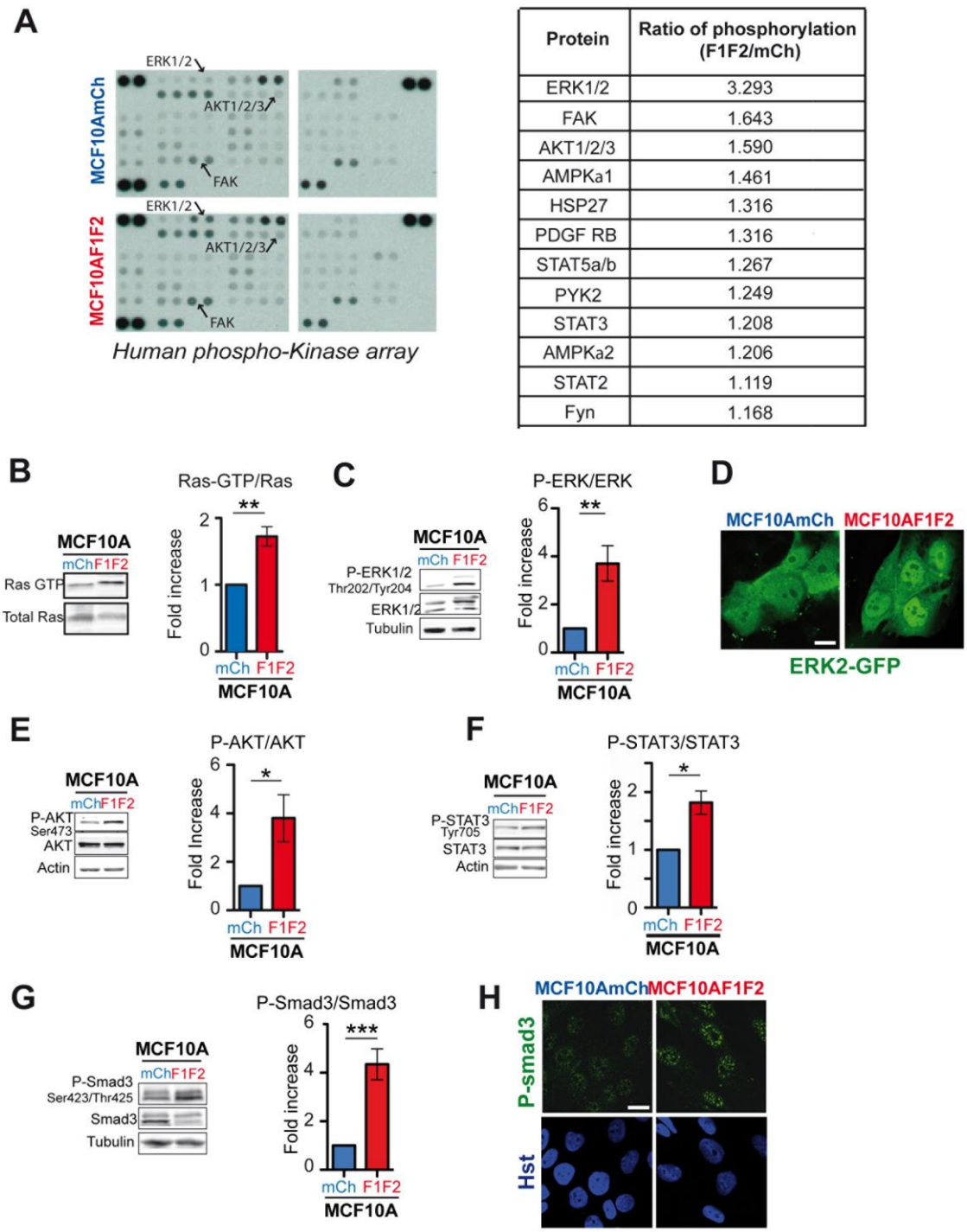

Protein	Ratio of phosphorylation (F1F2/mCh)
ERK1/2	3.293
FAK	1.643
AKT1/2/3	1.590
AMPKa1	1.461
HSP27	1.316
PDGF RB	1.316
STAT5a/b	1.267
PYK2	1.249
STAT3	1.208
AMPKa2	1.206
STAT2	1.119
Fyn	1.168

Figure 3: Flotillin upregulation promotes activation of oncogenic signaling pathways
A) Human phospho-kinase arrays were incubated with MCF10AmCh and MCF10AF1F2 cell lysates as described by the manufacturer. One representative example of arrays is shown. The table lists the twelve kinases and kinase substrates with the highest ratio of phosphorylation change between MCF10AF1F2 and MCF10AmCh cells. Values are the mean of 2 independent experiments.
B) The level of active GTP-bound Ras was measured using GST-Raf-RBD in lysates obtained from MCF10AmCh and MCF10AF1F2 cells. The histogram shows the mean value (± SEM) of Ras activity normalized to the amount of total protein calculated from 5 independent experiments.
C, E, F, G) Cell lysates from MCF10AmCh and MCF10AF1F2 cells were analyzed by western blotting to assess the phosphorylation status of the signaling proteins ERK1/2 (C, n=4), AKT (E), STAT3 (F), and Smad3 (G), with the indicated antibodies. The histograms show the mean value (± SEM) of protein

phosphorylation normalized to the total amount of the considered protein in MCF10AF1F2 cells compared with control MCF10AmCh cells calculated from 4 independent experiments.
D) MCF10AmCh and MCF10AF1F2 cells were transfected with an ERK2-GFP plasmid and ERK2-GFP distribution was analyzed by confocal microscopy at 36 hours post-transfection.
H) Confocal microscopy images of MCF10AmCh and MCF10AF1F2 cells incubated with an antibody against Smad3 phosphorylated on S423/425 and Hoechst (Hst) staining for nuclei.
In D and H, scale bars: 10µm. *P<0.05; **P<0.01; ***P<0.001

Flotillin upregulation in non-tumoral mammary epithelial cells activates several PM receptors that accumulate in flotillin-positive late endosomes.

To identify how flotillin upregulation in non-tumoral mammary cells activates these oncogenic signaling pathways, we used a Phospho-RTK array that allows the simultaneous screening of 49 tyrosine-phosphorylated RTKs. The tyrosine phosphorylation of 11 RTKs was increased by more than 1.4-fold in MCF10AF1F2 cells compared with MCF10AmCh cells (Fig. 4 A-B).

As signaling, endocytosis and vesicular trafficking are tightly connected processes (*6*, *8*, *27*) and flotillin upregulation stimulates the endocytosis of several cargos through the UFIT pathway (*13*, *16*, *28*, *29*), we analyzed the impact of flotillin upregulation on the trafficking of AXL, EphA4 the two top RTKs with increased tyrosine phosphorylation and of TGF-β receptor (TGF-β-R), in MCF10AF1F2 cells.

In MCF10AmCh cells, AXL was mainly expressed at the PM. In MCF10AF1F2 cells, AXL was still detectable at the PM in flotillin-rich regions, but was also enriched in flotillin-positive vesicles (Fig. 4 C). Similarly, in MDA-MB-231 mammary tumor cells, AXL and flotillin 2 colocalized at the PM and in intracellular vesicles (Fig. 4 D). Flotillin-positive endosomes are non-degradative late endosomes that contain LAMP-1, Rab7a and CD63 (*16*). In agreement, we found endogenous AXL and Myc-tagged AXL in flotillin-positive vesicles that contained and LAMP1 (Fig. S4 A) and CD63 (Fig. 4 E, S4 B). In living cells, AXL-GFP (see Fig. S 6 for its characterization) co-trafficked with flotillin 2-mCherry in MCF10AF1F2 and in MDA-MB-231 cells (Fig. 4 F and S4 C; Videos 1 and 2).

In NMuMGF1F2 cells, endogenous EphA4 strongly relocated from the PM to flotillin 2-mCherry- and CD63-positive vesicles compared with NMuMGmCh cells (Fig. 4 G and H). Due to the poor immunofluorescence detection of endogenous EphA4 in MCF10AF1F2 cells, we expressed EphA4-GFP and observed its accumulation in flotillin-positive late endosomes that contained LAMP1 (Fig. 4 I) and its co-trafficking with flotillin 2 (Fig. S4 D). Similarly, co-expression of TGF-β-RI-GFP and TGF-β-RII-Flag (the two TGF-β–R subunits) showed that they co-localized in flotillin- and CD63-positive vesicles (Fig. 4 J and S4 E, F). We could not detect all membrane receptors in flotillin-positive late endosomes. For instance, the transferrin receptor CD71 was not present in these compartments (Fig. S4 G).

Altogether, these data show that the UFIT pathway is associated with RTK activation and is sufficient to induce the accumulation of AXL, EphA4 and TGF-β-R in flotillin-positive late endosomes.

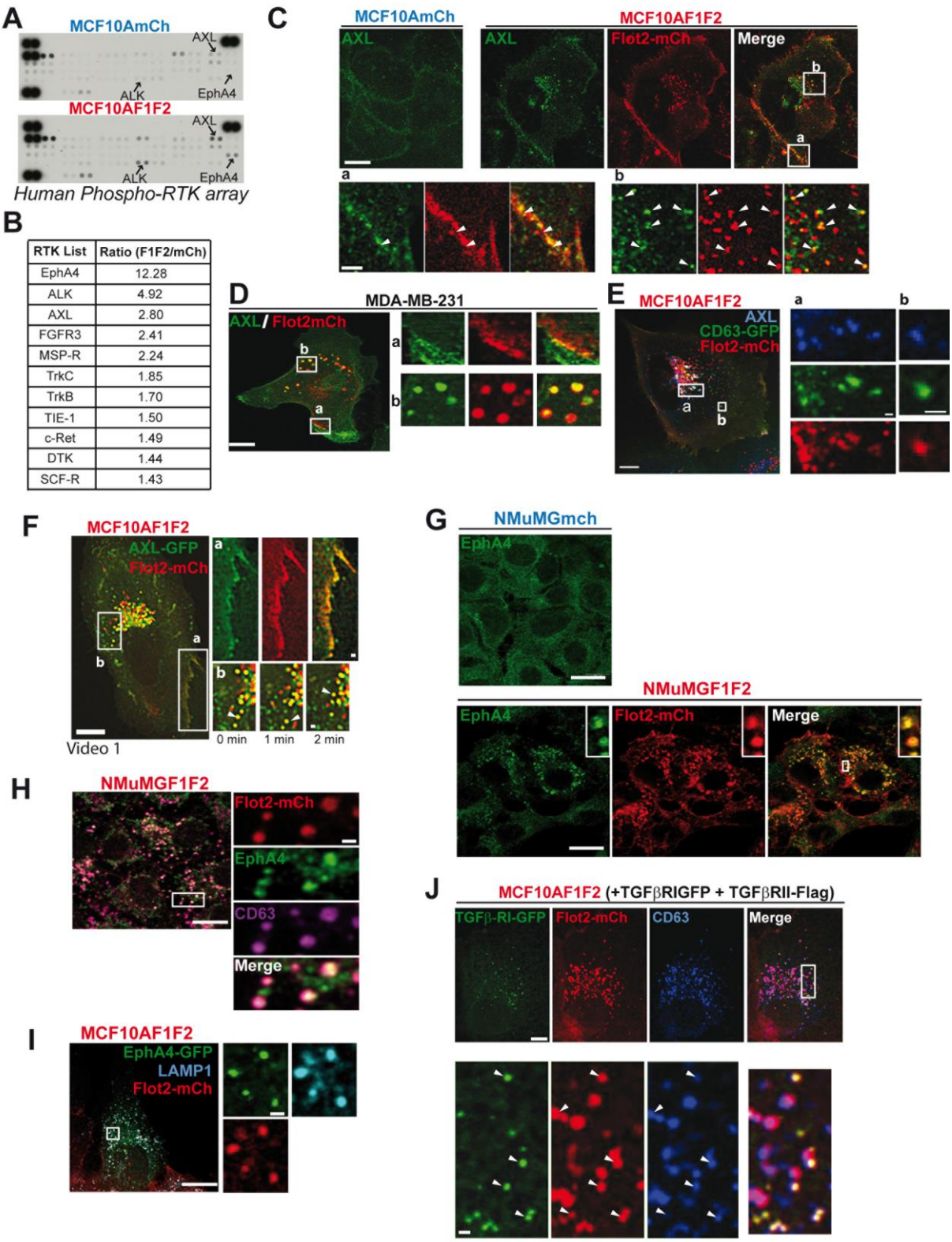

RTK List	Ratio (F1F2/mCh)
EphA4	12.28
ALK	4.92
AXL	2.80
FGFR3	2.41
MSP-R	2.24
TrkC	1.85
TrkB	1.70
TIE-1	1.50
c-Ret	1.49
DTK	1.44
SCF-R	1.43

Figure 4: Flotillin upregulation increases the activation of several RTKs located in flotillin-positive late endosomes.

A) *Flotillin upregulation increases the phosphorylation level of several RTKs.* Human phospho-Receptor Tyrosine kinase arrays were incubated with 200 µg of MCF10AmCh or MCF10AF1F2 cell lysates (cultured in the presence of serum) and processed as described by the manufacturer. One array example is shown.

B) List of the 11 RTKs with the highest increase in phosphorylation in MCF10AF1F2 compared with MCF10AmCh cells (data from 2 independent experiments).
C, D) *Flotillin upregulation modifies AXL cell distribution.* Distribution of endogenous AXL in MCF10AmCh and MCF10AF1F2 cells (C) and in MDA-MB-231 cells that co-express flotillin 1-HA and flotillin 2-mCherry (D) analyzed by confocal microscopy after immunofluorescence staining. Higher magnification images of the two boxed regions show AXL colocalization with flotillin 2-mCherry at the PM (a) and in intracellular vesicles (b). White arrows indicate some vesicles positive for both AXL and flotillin 2-mCherry.
E) *AXL is present in flotillin- and CD63-positive vesicles.* Immunofluorescence analysis of endogenous AXL expression in MCF10AF1F2 cells that express CD63-GFP by confocal microscopy. Higher magnification images of the two boxed regions show the presence of AXL in flotillin 2-mCherry- and CD63-positive vesicles.
F) *Co-trafficking of AXL and flotillins in MCF10AF1F2 cells.* Still images of a representative time-lapse series (video 1) of a MCF10AF1F2 cell that expresses AXL-GFP to illustrate the co-localization of AXL-GFP and flotillin 2-mCherry at the PM (box a), and in intracellular vesicles (box b) and their co-trafficking. The white arrow allows following one vesicle over time.
G, H) Immunofluorescence analysis of NMuMGmCh and NMuMGF1F2 cells to detect endogenous EphA4. In NMuMGF1F2 cells, EphA4 relocated in intracellular vesicles, many of which were flotillin 2-mCherry and CD63-positive (H).
I) Confocal microscopy image of one MCF10AF1F2 cell that expresses EphA4-GFP and stained for LAMP1, showing flotillin 2/EphA4 co-localization in LAMP-1-positive vesicles. The image is representative of several cells observed in independent experiments.
J) MCF10AF1F2 cells that co-express TGFβ-RI-GFP and TGFβ-RII-Flag were stained for CD63 and imaged by confocal microscopy. White arrows in the magnified images of the boxed area indicate co-localization of TGFβ-RI-GFP, CD63 and flotillin 2-mCherry in intracellular vesicles.
In panels C-J, scale bars: 10µm in the main images and 1 µm in the magnified regions.

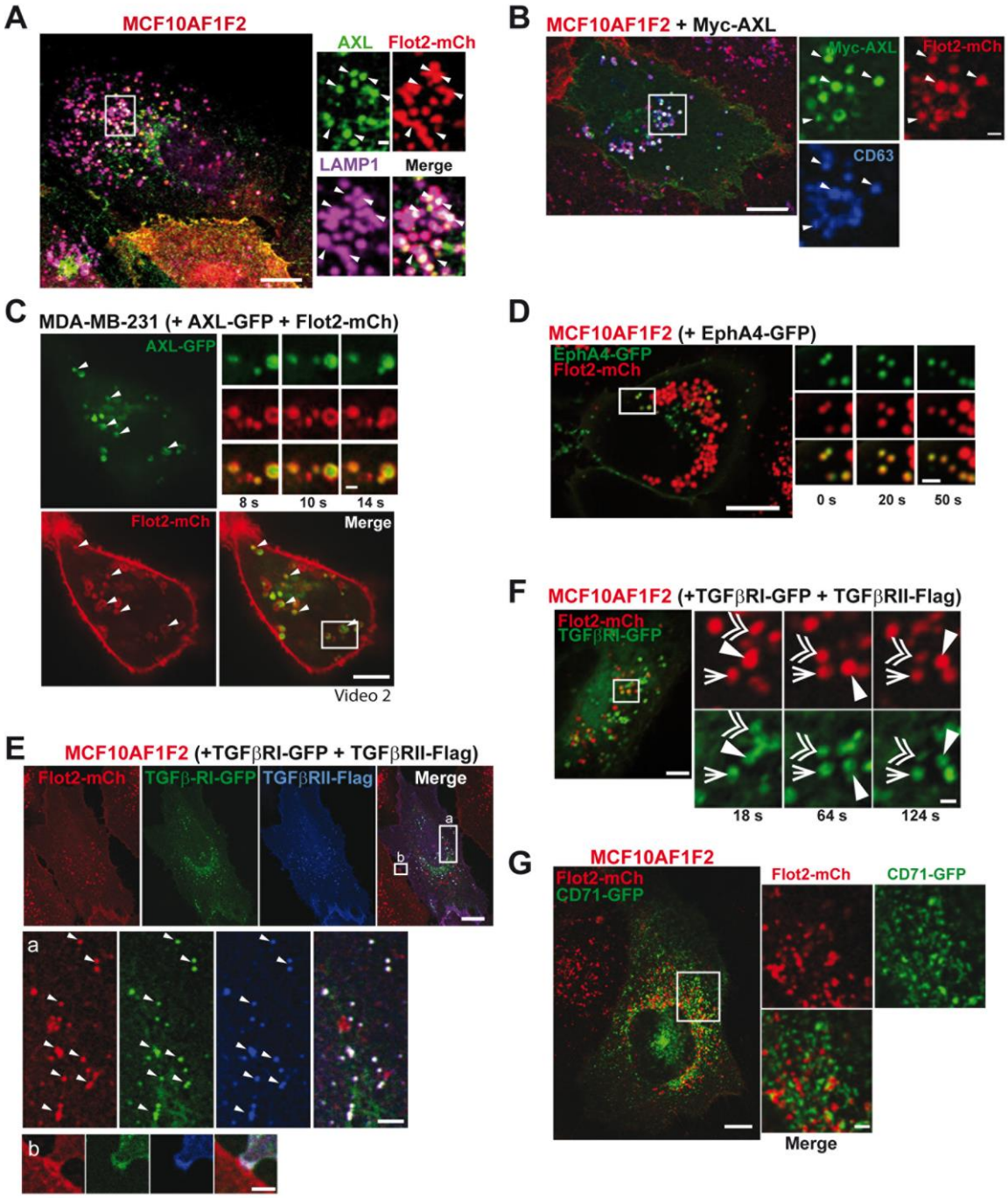

Figure S4: AXL, EphA4 and TGFβ receptor, but not CD71 relocate to flotillin-positive late endosomes in mammary epithelial cells upon flotillin upregulation.

A) In MCF10AF1F2 cells, endogenous AXL is localized in flotillin 2-mCherry vesicles positive for the endolysosomal marker LAMP1. Confocal microscopy image representative of several cells from independent immunofluorescence experiments.

B) Myc-tagged AXL expressed in MCF10AF1F2 cells is localized in flotillin 2-mCherry vesicles positive for the late endosomal marker CD63. Confocal microscopy image representative of several cells from independent immunofluorescence experiments.

C) MDA-MB-231 cells were transfected with AXL-GFP, flotillin 2-mCherry and flotillin 1-HA-encoding plasmids. Live cells were imaged by spinning disk confocal microscopy, showing the co-localization (indicated by white arrows) and the co-trafficking of AXL-GFP and flotillin 2-mCherry in intracellular vesicles (See also video 2).

D) Still images of a spinning disk confocal video of a MCF10AF1F2 cell that expresses EphA4-GFP showing the co-localization of EphA4-GFP and flotillin 2-mCherry. Images shown are representative of several cells observed in independent experiments.
E) MCF10AF1F2 cells that co-express the TGFβ-RI (GFP tagged) and TGFβ-RII (Flag tagged) subunits were analyzed by immunofluorescence using an anti-Flag antibody and imaged by confocal microscopy. Both subunits were concomitantly found at the PM and in intracellular vesicles (white arrows) where they colocalized with flotillin 2-mCherry. The image shown is representative of 3 independent experiments. Scale bars: 10 µm for all images, and 2 µm for the magnified images from the boxed area.
F) Spinning disk confocal still images of one MCF10AF1F2 cell that co-expresses TGFβ-RI-GFP and TGFβ-RII-Flag, showing the co-localization of TGFβ-RI-GFP and flotillin 2-mCherry in intracellular vesicles. The different arrows follow three distinct vesicles over time. Scale bars: 10 µm for all images, and 2 µm for the magnified images from the boxed area.
G) Transferrin receptor is not detected in flotillin-positive late endosomes. MCF10AF1F2 cells that express CD71-GFP were imaged by confocal microscopy. The image shown is representative of several cells in independent experiments. Scale bars: 10 µm in the main image and 2 µm in magnified images from the boxed area.

Flotillin-positive late endosomes act as signaling endosomes

The presence of AXL, EphA4 and TGF-β-R in flotillin-positive late endosomes led us to ask whether these vesicles are signaling endosomes. We detected active EphA4 (using an antibody against EphA4 phosphorylated at Y588/596) mainly at the PM in MCF10AmCh cells, but almost exclusively in flotillin 2-positive vesicles in MCF10AF1F2 cells (Fig. 5 A). As the antibody against AXL phosphorylated at Y702 could not detect endogenous AXL, we ectopically expressed Myc-tagged AXL in MCF10AF1F2 cells, and found it active (revealed with the antibody against AXL phosphorylated at Y702) both at the PM and in flotillin-positive vesicles (Fig. 5 B). We next focused on Ras, a key protein involved in signal transmission from RTKs to the ERK/MAPK and PI3-K/AKT pathways and activated upon flotillin upregulation (Fig. 3 B and E, and S1 L). We separately expressed the GFP-tagged H-Ras, N-Ras, K-Ras4A and K-Ras4B isoforms in MCF10AmCh and MCF10AF1F2 cells (Fig. 5 C and S5). Flotillin upregulation modified the distribution of only K-Ras4B but not of the other Ras isoforms. Indeed, K-Ras4B was localized at the PM in MCF10AmCh cells, and in flotillin-positive vesicles in MCF10AF1F2 cells (Fig. 5 C, video 3). Interestingly, this correlated with the co-immunoprecipitation of K-Ras4B, but not K-Ras4A, with flotillin 1 (Fig. 5 D).

In conclusion, the presence of activated receptors and of K-Ras4B indicate that flotillin-positive vesicles are signaling endosomes.

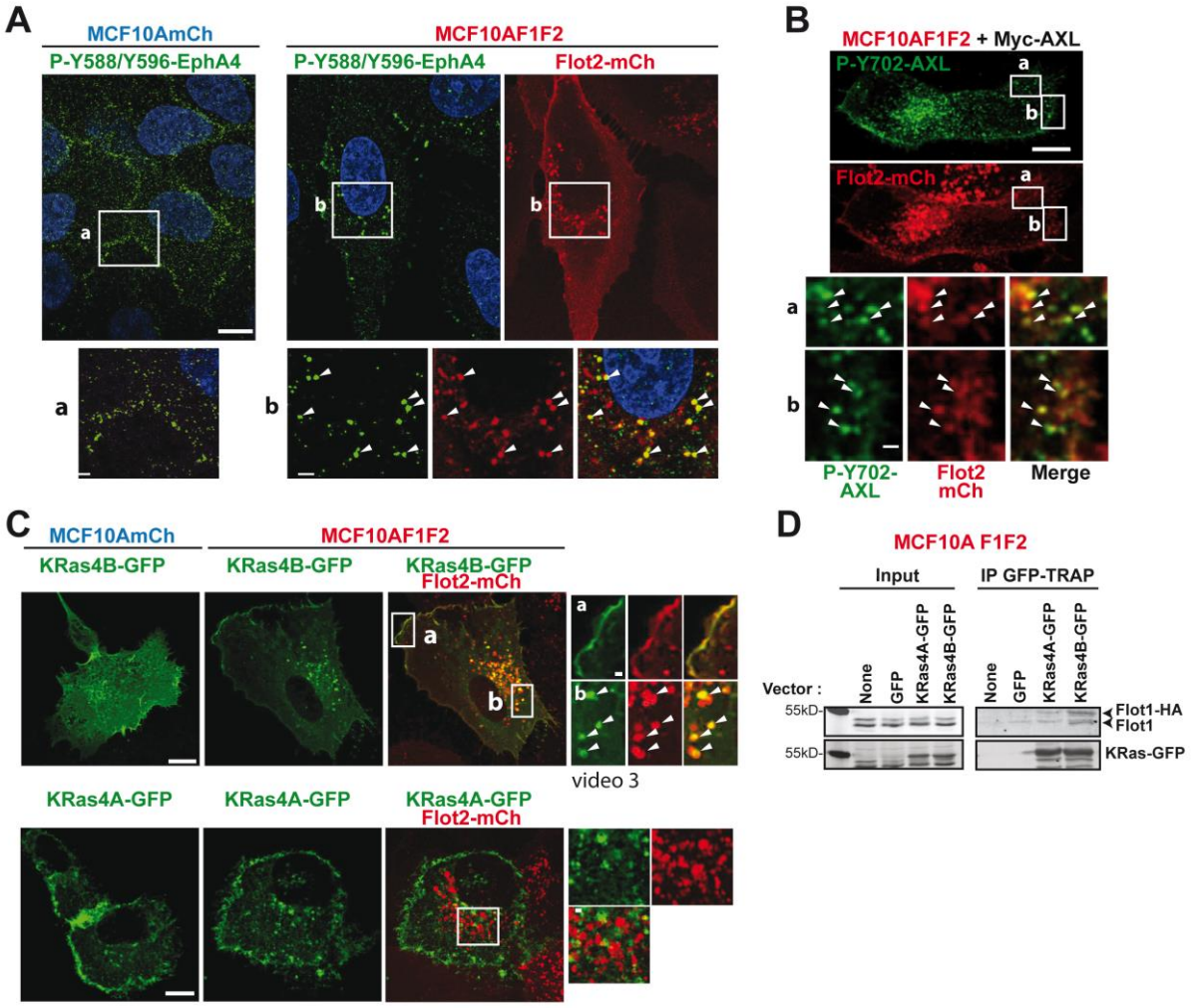

Figure 5: Flotillin upregulation promotes the formation of flotillin-positive signaling late endosomes that contain activated RTKs and K-Ras4B.

A) MCF10AmCh and MCF10AF1F2 cells analyzed by immunofluorescence using an antibody against EphA4 phosphorylated on Y588/Y596. In MCF10AmCh cells the signal was at cell-cell contacts (magnified image from the boxed area (a)), whereas it was concentrated in intracellular vesicles in MCF10AF1F2 cells where it co-localized with flotillin 2-mCherry (magnified images from boxed areas (b)).

B) *Flotillin-positive vesicles contain activated AXL.* Immunofluorescence analysis of endogenous AXL phosphorylated at Y702 in MCF10AF1F2 cells that express Myc-AXL imaged by confocal microscopy. The magnified images of the two boxed regions show AXL phosphorylated at Y702 in flotillin 2-mCherry-positive vesicles, some of them marked with white arrows.

C) *Flotillin upregulation specifically relocates KRas4B to flotillin-positive endosomes.* Confocal images of MCF10AmCh and MCF10AF1F2 cells that express KRas4A-GFP or KRas4B-GFP. In contrast to KRas4A-GFP (lower panels), KRas4B-GFP (upper panels) co-localized with flotillins and its distribution was modified in MCF10AF1F2 cells compared with MCF10AmCh cells (upper panel). KRas4B-GFP was mainly present at the PM in MCF10AmCh cells. Conversely, in MCF10AF1F2 cells, it remained visible at the PM where it co-localized with flotillin 2m-Cherry (magnified images from

boxed region (a)), but it was also strongly recruited to flotillin 2-mCherry-positive vesicles and co-trafficked with flotillin 2 (magnified images of the boxed region (b), and video 3).
D) *KRas4B forms a complex with flotillin 1.* Lysates from MCF10AF1F2 cells that express GFP alone, KRas4A-GFP, or KRas4B-GFP were immunoprecipitated with GFP-TRAP. Immunoprecipitates were probed by western blotting using anti-flotillin 1 and anti-Pan-Ras antibodies. Both KRas isoforms were expressed and immunoprecipitated at the same level. The signal for flotillin 1-HA and flotillin 1 in precipitates from KRas4B-GFP-expressing cells was clearly higher than the signal observed in precipitates from KRas4A-GFP-expressing cells that was similar to the background signal found in precipitates from GFP-expressing cells. Results shown are representative of 3 independent experiments. Scale bars: 10 µm in the main images and 2 µm in the magnified images.

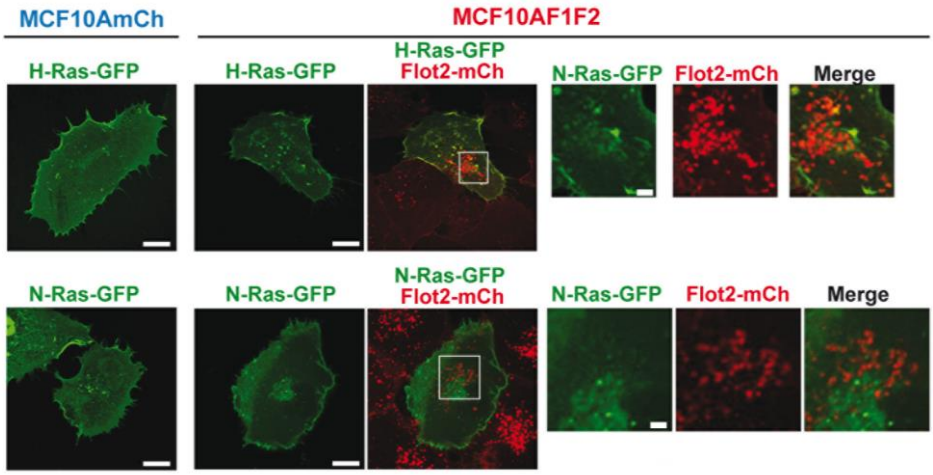

Figure S5: N-Ras and H-Ras distribution is not affected by flotillin upregulation.
Confocal images of MCF10AmCh and MCF10AF1F2 cells that express H-Ras-GFP or N-Ras-GFP. The distribution of these isoforms was not altered by flotillin upregulation. H-Ras-GFP was occasionally found in flotillin 2-mCherry-positive vesicles, but this was very rare for N-Ras-GFP. Images are representative of 3 independent experiments. Scale bars: 10 µm in the main images, and 2 µm in the magnified images from the boxed area.

Flotillin upregulation promotes AXL endocytosis toward flotillin-positive endosomes, leading to its stabilization.

Aberrant AXL expression is linked to EMT, metastasis formation, and poor prognosis (*4*, *5*, *30*, *31*). To analyze AXL contribution to EMT induced by flotillin upregulation, we knocked down AXL in MCF10AF1F2 cells. This led to ZEB1 expression downregulation (Fig. 6 A, B) and reversed the E- to N-cadherin switch (Fig. 6 A, C), revealing that AXL plays a central role in EMT induction by flotillin upregulation in mammary epithelial cells.

To characterize the impact of the UFIT pathway on AXL trafficking, we first determined whether AXL could be recruited to flotillin-positive microdomains at the PM. We developed an optogenetic approach based on the CRY2-CIBN system (*32*) to force flotillin oligomerization by light illumination (see Fig. S6 for the description of the experimental set-up) combined with total internal reflection fluorescence (TIRF) video-microscopy. Using MCF10A cells that express flotillin 2-CIBN-mCherry, CRY2-mCitrin and AXL-Halo, we demonstrated that upon light illumination to induce CRY2 oligomerization and binding to CIBN (*32*), domains that contained both flotillin 1 and 2 (Fig. S6 D) and AXL-Halo were formed at the PM (Fig. 6 D, S6, video 4). Moreover, using time-lapse imaging we could detect the concomitant endocytosis of flotillin 2-mCherry and AXL-GFP from PM sites of MCF10AF1F2 cells where both proteins initially co-accumulated (Fig. 6 E, video 5). These data, together with the demonstration of flotillin/AXL colocalization in late endosomes (Fig. 4 C-E), identified AXL as a cargo of the UFIT pathway. This is in agreement with the detection of flotillin 1 and AXL complexes by co-immunoprecipitation experiments (Fig. 6 F).

Then, we used a cell surface biotinylation assay to investigate the impact of the UFIT pathway in AXL internalization. We found that AXL internalization rate was significantly increased in MCF10AF1F2 cells compared with MCF10AmCh cells (Fig. 6 G, left panels). Conversely, in MDA-MB-231 cells, flotillin downregulation (shFlot2) slowed down AXL internalization (Fig. 6 G, right panels). In agreement, AXL accumulated at the PM in shFlot2-MDA-MB-231 cells (Fig. S7 A,B), but its global level remained unchanged (Fig. S7 C). We also performed an AXL uptake assay using the D4 antibody against the extracellular domain of human AXL (see validation in Fig. S7 D) to monitor AXL internalization by immunocytochemistry. The cell surface AXL signals were similar in MCF10AmCh and MCF10AF1F2 cells (Fig. S7 E). Conversely, after 10 min of internalization, the AXL-D4 signal was still mostly at the surface in MCF10AmCh cells, whereas it was clearly in flotillin-positive endosomes in MCF10AF1F2

cells (Fig. S7 E). We obtained similar results using an uptake assay where AXL surface expression was monitored with an anti-Myc antibody in cells transfected with N-terminally Myc-tagged AXL (Fig. S7 F). In contrast, CD71 internalization was not affected by flotillin upregulation (Fig. S7 G), in agreement with its absence in flotillin-positive vesicles (Fig. S4 G). Altogether, these results demonstrated that the UFIT pathway increases AXL internalization towards flotillin-positive endosomes.

We next analyzed the impact of the UFIT pathway on AXL expression level. The increase in AXL phosphorylated at Y702 of AXL in MCF10AF1F2 cells compared to MCF10AmCh cells (2.53 ± 0.71-fold increase) was due to a higher expression (2.57 ± 0.61 – fold increase) of AXL protein level (Fig. 6 H). Conversely, CD71 expression was comparable in both cell lines (Fig. S7 H). AXL increase was not explained by a flotillin effect on AXL transcription because AXL mRNA level was reduced in MCF10AF1F2 cells compared with MCF10AmCh cells (Fig. 6 I). To assess whether the higher level of AXL in MCF10AF1F2 cells was due to its stabilization, we compared AXL expression in MCF10AmCh and MCF10AF1F2 cells incubated with cycloheximide (CHX) to block protein synthesis. AXL expression was decreased by 50% after 1.9h and 6.8h of incubation with CHX in MCF10AmCh and in MCF10AF1F2 cells, respectively, indicating that flotillin upregulation promotes AXL stabilization (Fig. 6 J).

Altogether, these data demonstrated that AXL is crucial for EMT induced by flotillin upregulation. Moreover, flotillin upregulation stabilized active AXL by promoting its endocytosis in flotillin-positive late endosomes. Interestingly, we observed the co-expression of flotillin 1 and AXL in invasive breast tumor cells (Fig S8).

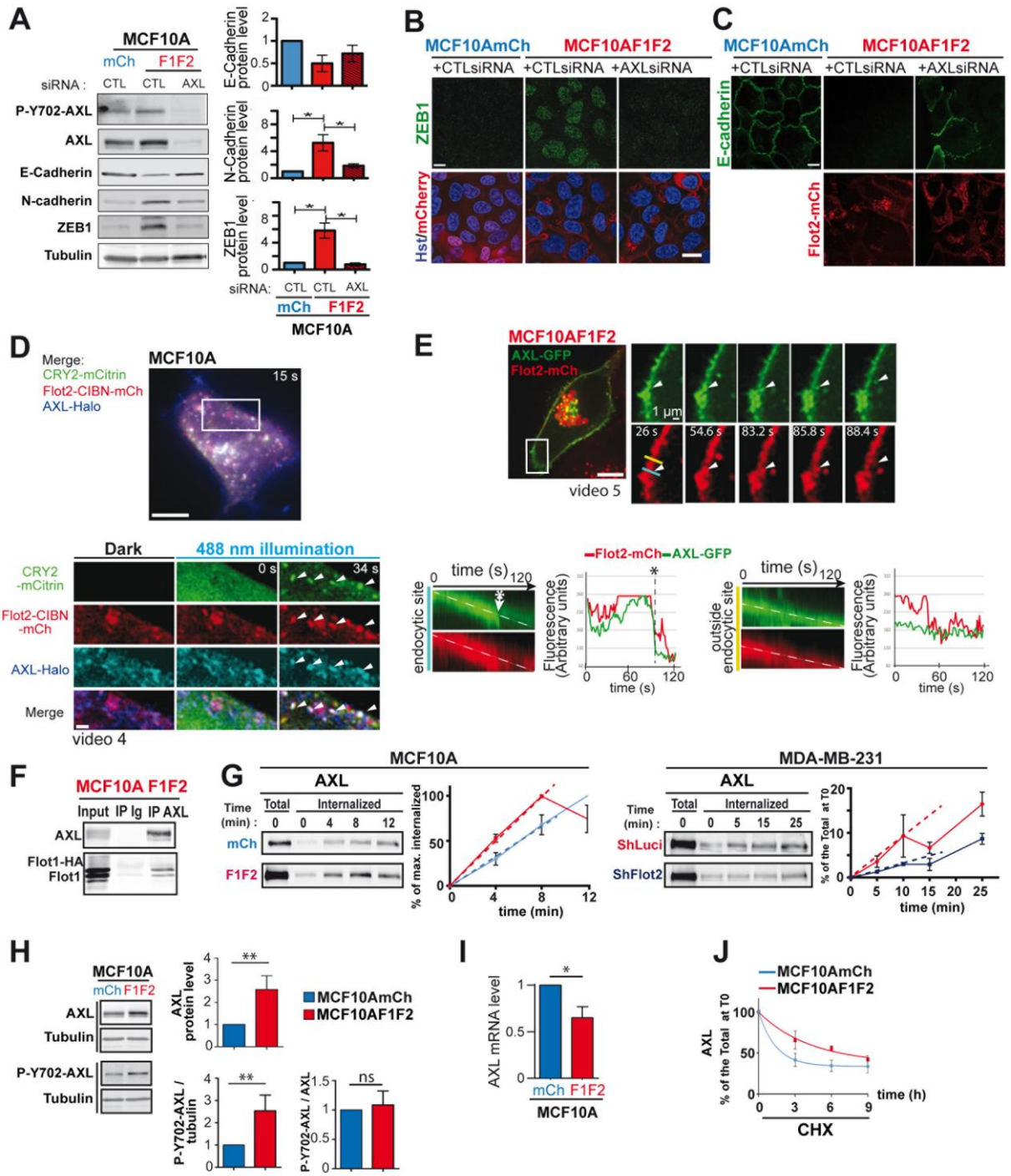

Figure 6: Flotillin upregulation stimulates AXL endocytosis towards non-degradative late endosomes and promotes its stabilization.

A) *AXL knock-down in MCF10AF1F2 cells decreases ZEB1 and N-cadherin expression*. MCF10AmCh and MCF10AF1F2 cells were transfected with control siRNA (CTL) or against AXL and probed by western blotting with antibodies for the indicated proteins. The quantification results are the mean ± SEM of 4 independent experiment, and are expressed as fold-increase compared with control (MCF10AmCh).

B) ZEB1 nuclear localization analyzed by immunocytochemistry and co-staining with Hoechst (Hst) and **C)** E-cadherin distribution analyzed by immunocytochemistry in MCF10AmCh and MCF10AF1F2 cells transfected with control (CTL) or anti-AXL siRNAs. Results shown are representative of 4 independent experiments. Scale bar: 10 µm.

D) *Flotillin-oligomerization induced by a CRY2-CIBN-based optogenetic approach promotes co-clustering of AXL*. Still images from a TIRF-microscopy movie of a MCF10A cell that co-expresses CRY2-mCitrin, flotillin 2-CIBN-mCherry, and AXL-Halo labeled with Halo-Tag-Janelia Fluor 646. Representative image of a whole cell 15s after starting the 488 nm illumination to perform CRY2 binding to flotillin 2-CIBN-mCh and subsequent oligomerization (see also supplementary Fig. S6 for the details regarding the validation of the constructs and the optogenetic approach). Magnified images from the boxed area taken before and after 488 nm illumination. Arrowheads indicate clusters of CRY2-mCitrin and flotillin 2-CIBN-mCherry where AXL-Halo accumulates (see also video 4). Scale bars: 10 µm for the main image and 2 µm for the images from the boxed area.
E) *Co-accumulation of AXL and flotillin 2 at the PM prior to their co-endocytosis*. Still images of a time-lapse series of one MCF10AF1F2 cell that expresses AXL-GFP to show flotillin 2/AXL co-localization at the PM and their co-endocytosis at PM sites (showed by arrowheads). Kymographs show the temporal variation of the GFP and mCherry signals along two line-scans (blue at the PM endocytic site, and yellow close to the PM endocytic site). Graphs show the intensity variation of both signals along the dotted white lines on the kymographs. The left kymograph shows the accumulation of AXL-GFP and flotillin 2-mCherry at the PM followed by a sudden concomitant drop of both signals (around 83s, indicated by a star). The right kymograph shows that in the meantime, both AXL-GFP and flotillin 2-mCherry signals remained stable at the PM outside and close to this endocytic site (See also video 5).
F) *Flotillin 1 co-precipitates with AXL.* AXL was immunoprecipitated from MCF10AF1F2 cell lysates, and flotillin 1 co-immunoprecipitation was assessed by immunoblotting. Control immunoprecipitation was performed with non-relevant immunoglobulins (Ig).
G) *Flotillin upregulation accelerates AXL endocytosis.* Kinetics of AXL internalization in MCF10AmCh and MCF10AF1F2 cells (left), and in MDA-MB-231shLuci and MDA-MB-231shFlot2 cells (right). Surface proteins were labeled with biotin at 4°C, and cells were incubated at 37°C for the indicated times to allow endocytosis. AXL presence in the internalized biotinylated fraction was probed by western blotting using relevant antibodies and quantified as the percentage of the maximum level of internalized protein (reached at 12 and 8 min, respectively, in MCF10AmCh and MCF10AF1F2 cells). Results are expressed as the mean ± SEM of 4 independent experiments. The AXL internalization rates (dashed lines) were 8.48 ± 1.28 and 12.43 ± 0.48 %/min in MCF10AmCh and MCF10AF1F2 cells, respectively, revealing a significant 1.45-fold increase ($p=0.0088$) upon flotillin upregulation. Comparison of the AXL internalization rates (dashed lines) in MDA-MB-231shLuci and MDA-MB-231shFlot2 cells showed a significant 3.66-fold decrease ($p=0.0009$) upon flotillin downregulation. Results are expressed as the percentage of the maximum level of surface labeled AXL at T0 and are the mean ± SEM of 4 independent experiments.
H) *Flotillin upregulation promotes AXL protein level increase*. Cell lysates from MCF10AmCh and MCF10AF1F2 cells were probed by western blotting with antibodies against AXL phosphorylated on Y702, AXL and tubulin. Results are expressed as fold-increase compared with MCF10AmCh cells and are the mean ± SEM of 6 independent experiments.
I) *Flotillin upregulation does not increase AXL mRNA level.* RT-qPCR analysis of AXL expression in MCF10AmCh and MCF10AF1F2 cells. Results are expressed relative to the level in MCF10AmCh cells and are the mean ± SEM of 4 independent experiments.
J) *Flotillin upregulation stabilizes AXL.* MCF10A and MCF10AF1F2 cells were incubated with cycloheximide (CHX, 100µg/ml) and cell lysates collected at the indicated time points. AXL and tubulin levels were assessed by western blotting. The graph shows the normalized AXL levels in each cell line during CHX incubation. CHX treatment was stopped after 9 hours because MCF10Amch cells did not survive longer treatment.
*$P<0.05$; **$P<0.01$

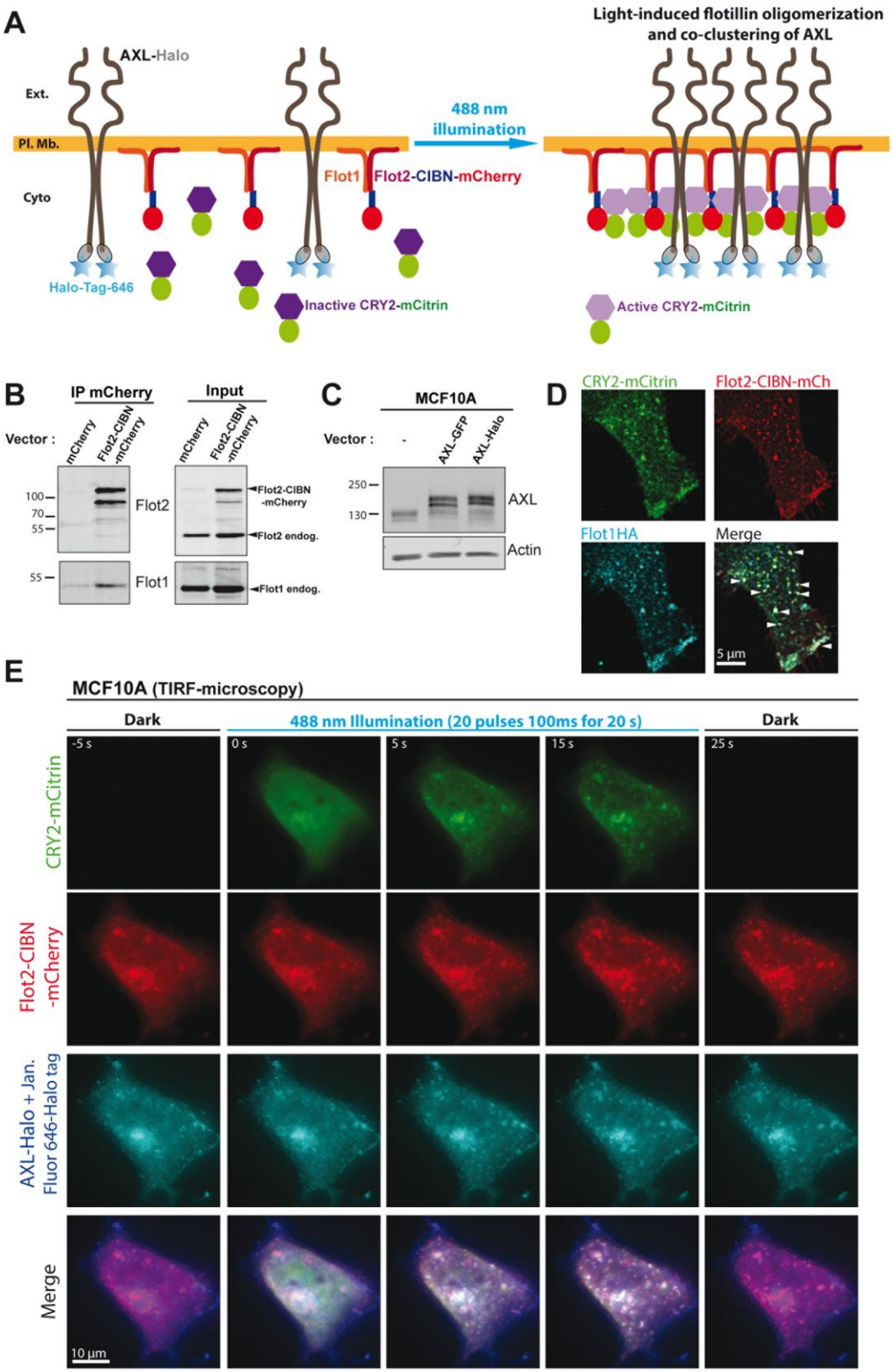

Figure S6: AXL clustering at membrane sites of flotillin oligomerization.
(A) *Schema describing the optogenetic system used to induce flotillin oligomerization.* Flotillin 2-CIBN-mCherry, CRY2-mCitrin and AXL-Halo labeled with Halo-Tag-Janelia Fluor 646 were co-expressed in MCF10A cells that express endogenous flotillins. Light illumination (488nm) induces the

oligomerization of "active" CRY2 and its binding to CIBN, allowing the oligomerization of flotillin 2-CIBN-mCherry with flotillin 1. AXL-Halo is trapped in the light-induced flotillin-microdomains.
(B) *Flotillin2-CIBN-mCherry interacts with flotillin 1.* Immunoprecipitations using an antibody against mCherry (mCherry trap) and lysates from MCF10A cells that express mCherry alone or flotillin 2-CIBN-mCherry. Immunoprecipitates were then analyzed with antibodies to detect flotillin 1 and 2. Flotillin 1 was co-immunoprecipitated only in lysates from cells that express flotillin 2-CIBN-mCherry, but not mCherry alone. Results are representative of 3 independent experiments.
(C) *Characterization of the AXL-GFP and AXL-Halo constructs.* MCF10A cells were transfected with empty vector (-) or plasmids encoding AXL-GFP or AXL-Halo. Expression of the proteins of the expected size (138+28=166 kDa for AXL-GFP) and (138+28=171 kDa for AXL-Halo) is shown. In both cases, the tagged proteins exhibit a doublet, as observed for endogenous AXL.
(D) *Light-induced flotillin 2-CIBN-mCherry microdomains contain flotillin 1.* MCF10A cells that co-express flotillin 2-CIBN-mCherry, flotillin 1-HA and CRY2-mCitrin were illuminated at 488 nm for 1 min, fixed, incubated with an anti-HA antibody and imaged by confocal microscopy. CRY2-mCitrin patches containing flotillin 2-CIBN-mCherry (white arrows) also exhibit flotillin 1-HA signal.
(E) Still images from a TIRF-microscopy video of one MCF10A cell that co-expresses CRY2-mCitrin, flotillin 2-CIBN-mCherry and AXL-Halo labeled with Halo-Tag-Janelia Fluor 646. The cell was imaged before, during, and after 488 nm illumination (22 pulses of 100 ms each every second).

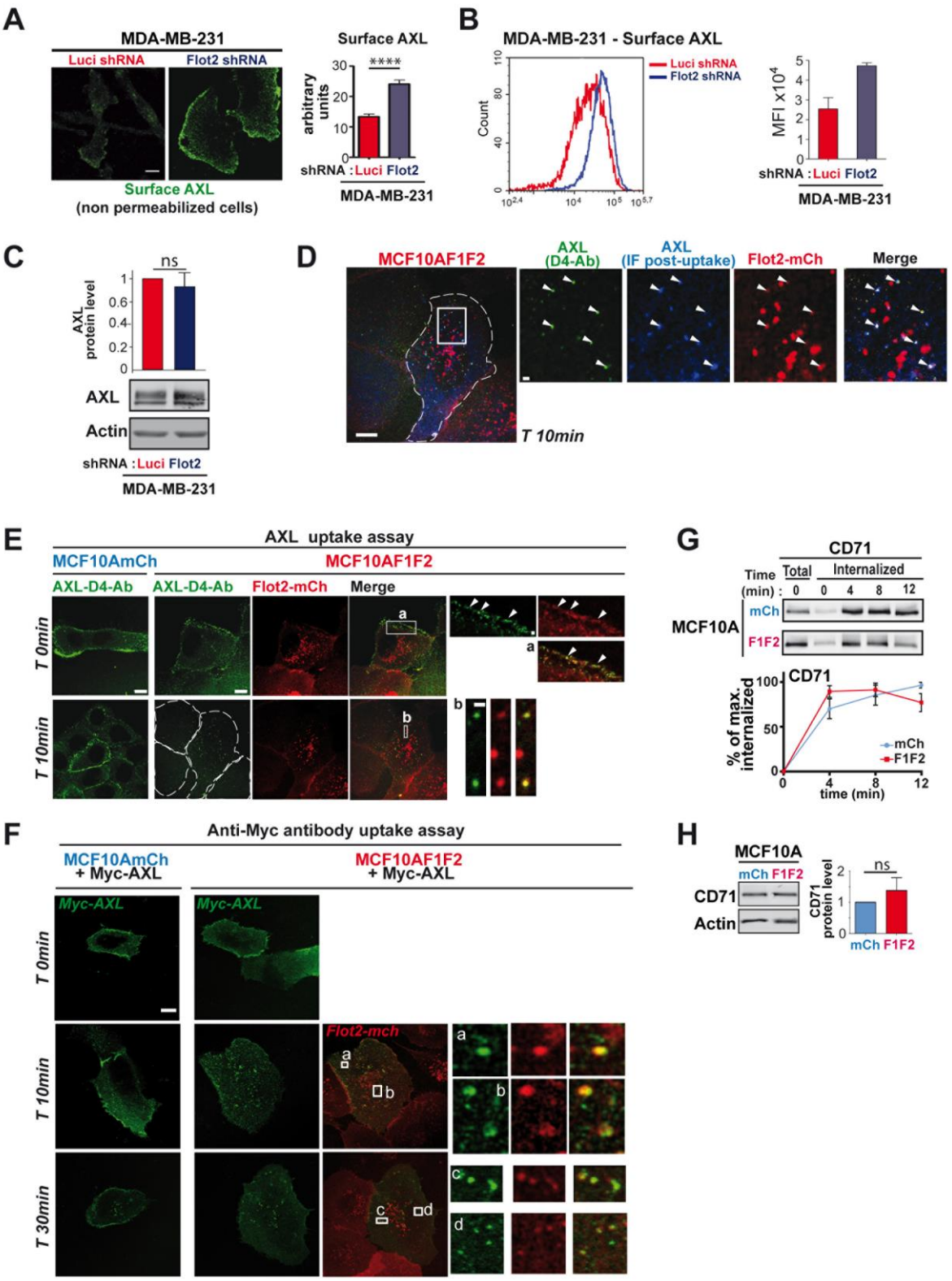

Figure S7: AXL surface staining in MDA-MB-231 cells and AXL and CD71 uptake.
A,B) *AXL level at the cell surface is increased in MDA-MB-231 cells in which flotillins were knocked down.* **(A)** In fixed non-permeabilized cells, AXL expression was analyzed using the monoclonal D4 antibody against AXL extracellular domain and an Alexa488-conjugated anti-human secondary antibody. Images were acquired in the same illumination conditions for MDA-MB-shLuci cells (control) and MDA-MB-231-shFlot2cells (in which flotillins were knocked down). Using the Fiji software, the mean fluorescence intensity was quantified in each area delimited by the cellular outline. Quantification

was done in 53 MDA-MB-shLuci cells and 41 MDA-MB-231-shFlot2cells. The values were expressed as arbitrary units correspond to the mean ± SEM. **(B)** AXL surface staining analyzed by FACS. Fixed, non-permeabilized cells were labeled with the D9 anti-AXL antibody and a Alexa488-conjugated secondary antibody and analyzed by FACS. Results are expressed as the Mean Fluorescence Intensity (MFI) from 3 independent experiments.
(C) AXL detection by western blotting in whole cell lysates of MDA-MB-231shLuci and shFlot2 cells. Actin was used as loading control. Results are expressed as fold-increase compared with MDA-MB-shLuci cells and are the mean ± SEM of 4 independent experiments.
D) MCF10AmCh and MCF10AF1F2 cells were incubated with the anti-AXL D4 antibody (against AXL extracellular domain) at 4°C followed by incubation at 37°C for 10 min to allow AXL internalization. After fixation and permeabilization, internalized AXL was labeled (green) with a FITC-conjugated secondary antibody directed against the D4 antibody. Immunofluorescence staining of AXL (blue) was also performed using an antibody against AXL cytoplasmic domain and an Alexa-633 conjugated secondary antibody. Arrowheads indicate flotillin 2-mCherry-positive vesicles in which AXL is internalized (green). Images are representative of at least 5 independent experiments.
E) MCF10AmCh and MCF10AF1F2 cells were incubated with the anti-AXL D4 antibody at 4°C followed by incubation at 37°C for 10 min to allow AXL internalization. AXL distribution and flotillin 2-mCherry signal were analyzed by immunocytochemistry. Arrowheads indicate AXL/flotillin 2 colocalization. Images are representative of at least 5 independent experiments. Scale bars are 10 µm in the main images, and 1 µm in the magnified images from the insets.
F) MCF10AmCh and MCF10AF1F2 cells that express Myc-tagged AXL were incubated with an anti-Myc antibody at 4°C followed by incubation at 37°C for the indicated time. Myc-AXL distribution was analyzed by immunocytochemistry using an Alexa488-conjugated secondary antibody. Scale bars = 10 µm in the main images, and 1 µm in the magnified images from the insets.
G) *Flotillin upregulation does not affect transferrin receptor endocytosis.* Kinetics of CD71 (transferrin receptor) internalization in MCF10AmCh and MCF10AF1F2 cells analyzed in the same experiments presented in Figure 6 G. Surface proteins were labeled with biotin at 4°C and cells incubated at 37°C for the indicated times to allow endocytosis. CD71 presence in the internalized biotinylated fraction was probed by western blotting using relevant antibodies, and quantified as the percentage of the maximum level of internalized protein. Results are expressed as the mean ± SEM of 4 independent experiments. The CD71 internalization rates were not significantly different between cell lines at 4, 8 and 12 min, $p>0.1$.
H) *Flotillin upregulation does not affect CD71 level.* Cell lysates of MCF10AmCh and MCF10AF1F2 cells were probed by western blotting with antibodies against CD71 and actin. Results are expressed as fold-increase compared with MCF10AmCh cells and are the mean ± SEM of 4 independent experiments.

A

Triple negative Breast tumor *(patient #2)*

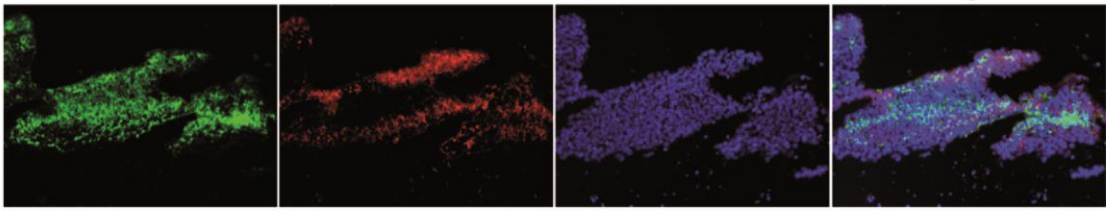

45% of Flotillin 1/AXL positive cells

Luminal (HR+/Erb2-) Breast tumor *(patient #2)*

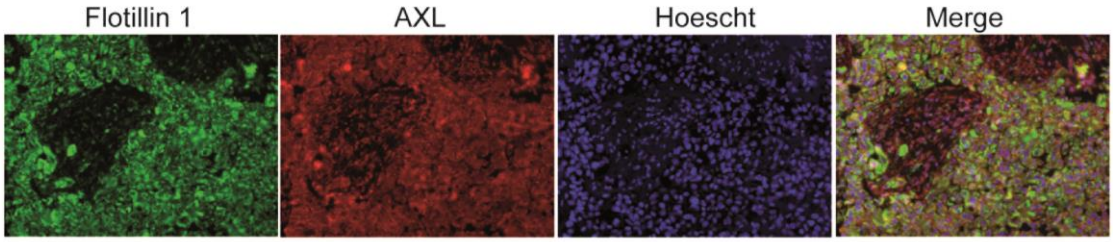

75% of Flotillin 1/AXL positive cells

HER2 Breast tumor *(patient #2)*

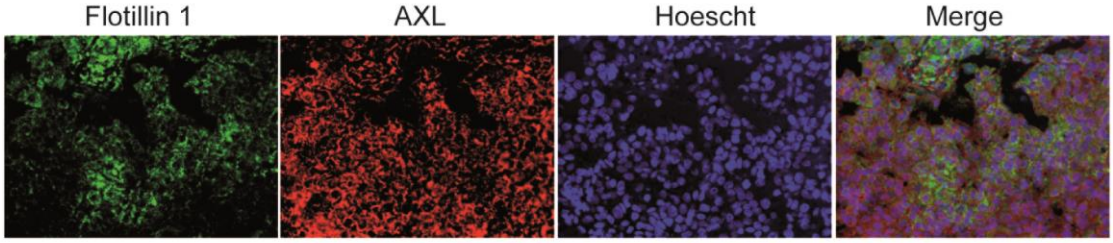

80% of Flotillin 1/AXL positive cells

B

Tumor type	Patient	Flotillin 1 expression	Flotillin 1/AXL co-expression (%)
Triple negative, IC, LN+	#1	no	2
Triple negative, IC, LN-	#2	yes	45
Triple negative, IC, LN-	#3	no	4
HR+/ERBB2-, IC, LN-	#1	yes	80
HR+/ERBB2-, IC, LN+	#2	yes	75
HR+/ERBB2-, IC, LN+	#3	yes	86
HR-/ERBB2+, IC, LN+	#1	yes	89
HR-/ERBB2+, IC, LN-	#2	yes	80
HR-/ERBB2+, IC, LN+	#3	no	17

Figure S8

Figure S8: ***Flotillin 1 and AXL are coexpressed in invasive breast tumor cells***
A) Immunofluorescence analysis of Flotillin 1 and AXL in invasive breast tumor tissue sections in one patient sample from each breast tumor subtype. Nuclei were stained with DAPI.
B) Nine breast samples were stained by immunofluorescence for flotillin 1 and AXL expression. Coexpression was calculated with the Vectra 3.0 Automated Quantitative Pathology Imaging System. IC, invasive carcinoma; LN, lymph node.

Sphingosine kinase 2 is required for AXL stabilization through the UFIT pathway

Because of the link between sphingolipid metabolism and endocytosis, and between sphingolipids and flotillins, we investigated the role of these lipids in the UFIT pathway. Indeed, flotillins bind to sphingosine, the S1P precursor, and S1P level is reduced in cells from flotillin knock-out mice (*33*). It has been reported that S1P, a bioactive lipid, is implicated in endocytosis and membrane remodeling (*34–36*). Moreover, S1P production induced upon sphingosine phosphorylation by SphK 1 or 2 has been linked to cancer progression (*37*). SphK 1/2 subcellular localization and consequently the compartmentalization of S1P production play an important role in their function (*38*).

To assess the localization of SphK isoforms in MCF10AF1F2 and MDA-MB-231 cells, we expressed GFP-tagged SphK1 and 2 because no antibody is available for immunofluorescence staining. In both cell lines, SphK1-GFP was present in the cytosol, at the PM, and in intracellular vesicles among which less than 20% were flotillin-positive (Fig. 7 A and B and S9 A). Conversely, we detected SphK2-GFP in approximately 70% of flotillin-positive vesicles (Fig. 7 A-D, video 6). SphK2- and flotillin-positive vesicles also contained AXL (Fig. 7 C, video 7), and the late endosomal markers Rab7 (Fig. S9 B) and CD63 (Fig. S9 C). Flotillin upregulation did not affect SphK2 protein expression level (Fig. S9 D), but increased its recruitment to CD63-positive late endosomes (Fig. S9 E). SphK2 and flotillin 2 also colocalized at discrete sites of the PM, from which we could observe the fast co-endocytosis of both proteins (Fig. 7 D, videos 8 and 9).

Due to SphK2 enrichment in flotillin-positive membrane domains and flotillin-positive vesicles, we asked whether SphK2 was involved in AXL stabilization upon flotillin upregulation. We first incubated cells with opaganib (ABC294640), a selective SphK2 inhibitor (*33*). Few minutes after opaganib addition, we observed the dissociation of SphK2-GFP from flotillin-positive endosomes that lasted for several hours (Fig. S9 F, video 10). Short time (4h) incubation with opaganib did not have any impact on AXL (Fig. 7 E and G). However, in MCF10AF1F2 cells incubated with opaganib for 10h, AXL level was reduced to that observed in MCF10AmCh cells (Fig. 7 E). AXL was similarly decreased in MCF10F1F2 cells where SphK2 was efficiently knocked down using siRNA (Fig. 7 F). In MDA-MB-231shLuci cancer cells that express high flotillin levels, SphK2 inhibition with opaganib also led to AXL decrease (Fig. 7 G). In both MCF10AF1F2 and MDA-MB-231shLuci cells, SphK2 inhibition decreased also ZEB1 level (Fig. 7 E-G), in agreement with our finding that its expression is dependent on AXL (Fig. 6 A and B). Of note, SphK2 inhibition did not alter flotillin 1 and 2 level (Fig. 7 E). On the other hand, SphK2 inhibition with opaganib did not affect AXL level in MCF10AmCh cells (Fig. 7 E) and in MDA-MB-231shFlot2 cells (Fig. 7 G), indicating that SphK2 activity is required for maintaining a high level of AXL specifically in the context of flotillin upregulation. We also investigated the potential involvement of SphK1. However, in agreement with the limited localization of SphK1-GFP in flotillin-positive vesicles (Fig. 7 B and S9 A), SphK1 inhibition using PF543 had no effect on AXL level in MCF10AF1F2 and MDA-MB-231 cells (Fig. S9 G).

To confirm that SphK2 was involved in AXL stabilization downstream of upregulated flotillins, we examined AXL levels in MCF10AF1F2 and MDA-MB-231shLuci cells incubated with CHX to inhibit protein synthesis. As expected CHX considerably decreased AXL level in both cell lines. This decrease was further reinforced by the co-treatment with Opaganib (Fig. 7

H), demonstrating that SphK2 activity was involved in AXL stabilization but not in stimulating its synthesis.

We next investigated how SphK2 was involved in AXL stabilization. SphK2 co-accumulated with flotillins at the PM prior to endocytosis (Fig. 7 D), suggesting its participation in flotillin-mediated AXL endocytosis. Therefore, we hypothesized that SphK2 inhibition could impair AXL internalization, leading to an increase of its expression at the cell surface. To this aim, we compared AXL expression at the PM in cells incubated or not (control) with opaganib for 4 hours because at this time point the global AXL decrease is not detectable yet (Fig. 7 E and G), thus allowing a comparative analysis of its amount at the cell surface. Quantification of AXL surface expression showed that it was increased at the PM in both MCF10AF1F2 and MDA-MB-231shLuci cells (Fig. 7 I and J), indicating that SphK2 participates in flotillin-mediated AXL endocytosis.

In conclusion, the lipid kinase SphK2 colocalizes with flotillins at the PM and in late endosomes, and is required to divert AXL endocytosis towards the UFIT pathway, thus promoting its stabilization.

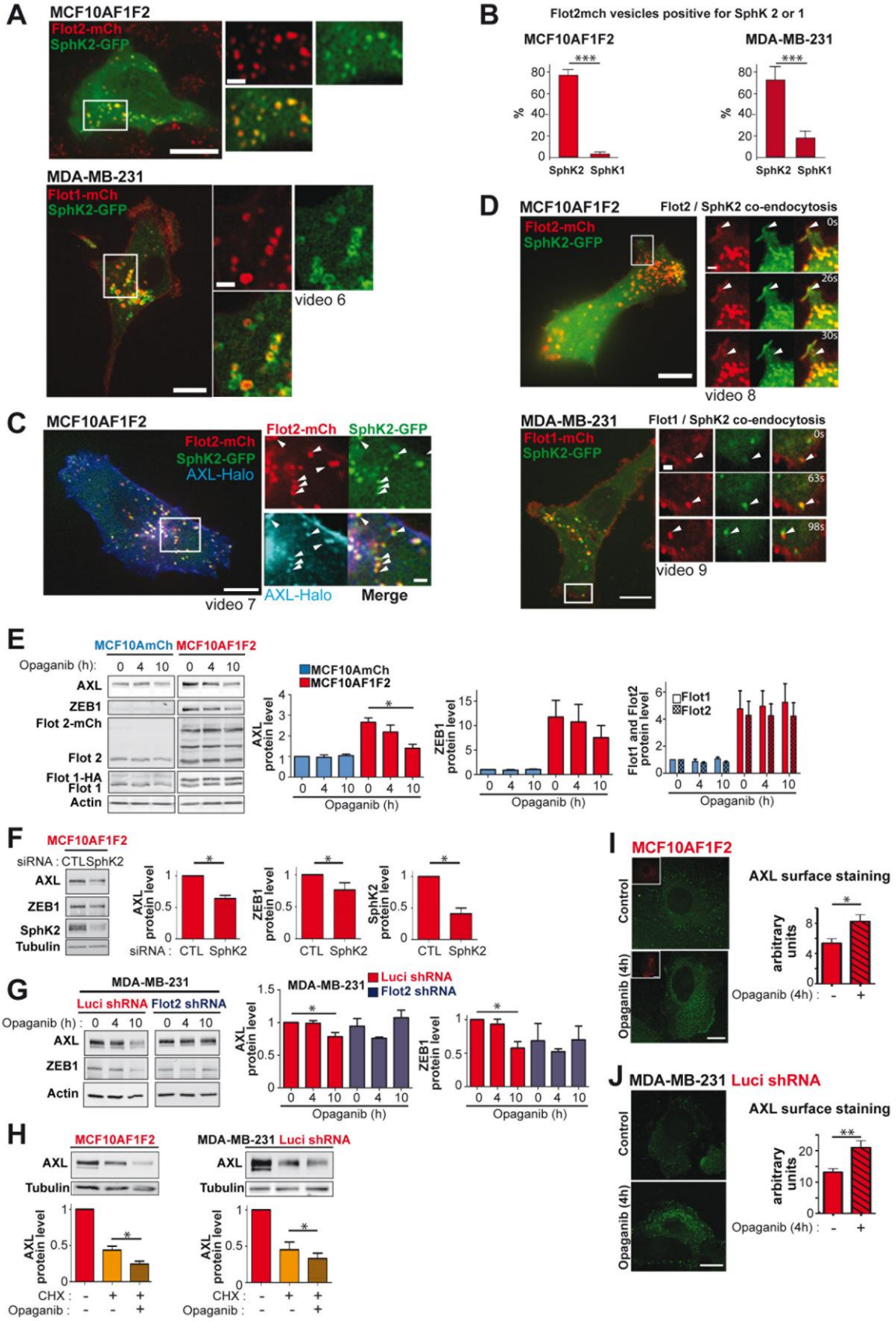
A
MCF10AF1F2
Flot2-mCh
SphK2-GFP
MDA-MB-231
Flot1-mCh
SphK2-GFP
video 6
B
Flot2mch vesicles positive for SphK 2 or 1
MCF10AF1F2
MDA-MB-231
***
%
SphK2 SphK1
C
MCF10AF1F2
Flot2-mCh
SphK2-GFP
AXL-Halo
video 7
Merge
D
MCF10AF1F2
Flot2 / SphK2 co-endocytosis
video 8
MDA-MB-231
Flot1 / SphK2 co-endocytosis
video 9
E
MCF10AmCh MCF10AF1F2
Opaganib (h): 0 4 10 0 4 10
AXL
ZEB1
Flot 2-mCh
Flot 2
Flot 1-HA
Flot 1
Actin
AXL protein level
ZEB1 protein level
Flot1 and Flot2 protein level
Flot1
Flot2
Opaganib (h)
F
MCF10AF1F2
siRNA : CTL SphK2
AXL
ZEB1
SphK2
Tubulin
AXL protein level
ZEB1 protein level
SphK2 protein level
siRNA : CTL SphK2
G
MDA-MB-231
Luci shRNA Flot2 shRNA
Opaganib (h) : 0 4 10 0 4 10
AXL
ZEB1
Actin
Luci shRNA
Flot2 shRNA
H
MCF10AF1F2
MDA-MB-231 Luci shRNA
AXL
Tubulin
AXL protein level
CHX :
Opaganib :
I
MCF10AF1F2
Control
Opaganib (4h)
AXL surface staining
arbitrary units
Opaganib (4h) : - +
J
MDA-MB-231 Luci shRNA
Control
Opaganib (4h)
AXL surface staining
arbitrary units
Opaganib (4h) : - +

Figure 7

Figure 7: Sphingosine kinase 2 is required for flotillin-induced AXL stabilization

A, B, D) *SphK2 is enriched in flotillin-positive late endosomes and co-accumulates at the PM with flotillins prior to endocytosis.* MCF10AF1F2 cells that expressing SphK2-GFP (A,B) and MDA-MB-231 cells that co-express flotillin 1-mCherry or flotillin 2-mCherry and SphK2-GFP (A,B,D) were imaged by spinning disk confocal microscopy (See also videos 6, 7, 8, 9). (**A,B**) *SphK2-GFP, but not SphK1-GFP is abundantly present in flotillin 2-mCherry-positive vesicles* (Fig. S9 A). Quantification of flotillin 2-mCherry-positive vesicles in which SphK2-GFP or SphK1-GFP is detected (B). Results are expressed as the percentage of vesicles and are the mean ± SEM (n=300 vesicles in 10 MCF10AF1F2 cells, and n=100 vesicles in 10 MDA-MB-231 cells that co-express flotillin 2-mCherry and SPK2 or SPK1-GFP). (D) *Fast co-endocytosis of flotillin 2-mCherry and SphK2-GFP following their co-accumulation at the plasma membrane* (indicated by the arrows) in MCF10AF1F2 cells (upper panel) and MDA-MB-231 cells (lower panel). Shown are still images from spinning disk confocal videomicroscopy.

C) *AXL is present in flotillin- and SphK2-positive vesicles.* Still image from spinning disk confocal microscopy of live MCF10AF1F2 cells that co-expressing SphK2-GFP and AXL-Halo labeled with Halo-tag-Janelia Fluor 646. Arrows show flotillin-positive vesicles that contain SphK2-GFP and AXL-Halo (See also video 7).

E) *SphK2 inhibition decreases AXL and ZEB1 levels in MCF10AF1F2 cells.* MCF10AmCh and MCF10AF1F2 cells were incubated with opaganib (50 µM) for the indicated times. AXL, ZEB1, flotillin 1 and 2 were analyzed by western blotting in whole cell lysates. Results correspond to the level of each protein normalized to the actin signal, expressed as the fold increase compared to control (MCF10AmCh cells) and are the mean ± SEM of 4 independent experiments.

F) *SphK2 downregulation decreases AXL and ZEB1 levels in MCF10AF1F2 cells.* MCF10AF1F2 cells were transfected with siRNAs against luciferase (CTL) or SphK2, and siRNA efficacy was tested by western blotting with antibodies against SphK2 and also AXL, ZEB1 and tubulin. Histograms show the level of each protein normalized to the tubulin signal, expressed as fold increase compared with CTL and are the mean ± SEM of 4 independent experiments.

G) *SphK2 inhibition decreases AXL and ZEB1 levels in MDA-MB-231 cells.* MDA-MB-231shLuci (control) and MDA-MB-231shFlot2 cells were incubated with opaganib (50 µM) for the indicated times. AXL, ZEB1 and actin were analyzed by western blotting in whole cell lysates. The histograms show the level of each protein normalized to the actin signal, expressed as fold increase compared with control and are the mean ± SEM of 5 independent experiments.

H) *AXL decrease upon SphK2 inhibition is not due to protein synthesis inhibition.* MCF10AF1F2 and MDA-MB-231shLuci cells were incubated or not with opaganib for 10 hours. When indicated, cycloheximide (CHX) was added 4 hours after the beginning of opaganib incubation. AXL was analyzed by western blotting in whole cell lysates. The histograms show the level of AXL normalized to the tubulin signal, expressed as fold increase compared with control (no treatment) and are the mean ± SEM of 4 independent experiments.

I,J) *SphK2 inhibition increases AXL level at the cell surface in flotillin-upregulated cells.* Fixed non-permeabilized cells were immunostained for AXL using the monoclonal D4 antibody against AXL extracellular domain and an Alexa488-conjugated anti-human secondary antibody. Images of control- and opaganib-treated cells (50µM, 4h) were acquired in the same conditions. Representative images are shown (for MCF10AF1F2 cells, the insets show flotillin 2-mCherry signal). The mean fluorescence intensity was quantified in the area defined by the outline of each individual cell. Results are expressed as arbitrary units and are the mean ± SEM of 23 measurements for MCF10AF1F2 cells (I), and 22 measurements for MDA-MB-231shLuci cells (J) for each condition (control and opaganib).

Scale bars: 10 µm for the main images and 2 µm in the magnified images from the boxed area. *P<0.05; **P<0.01.

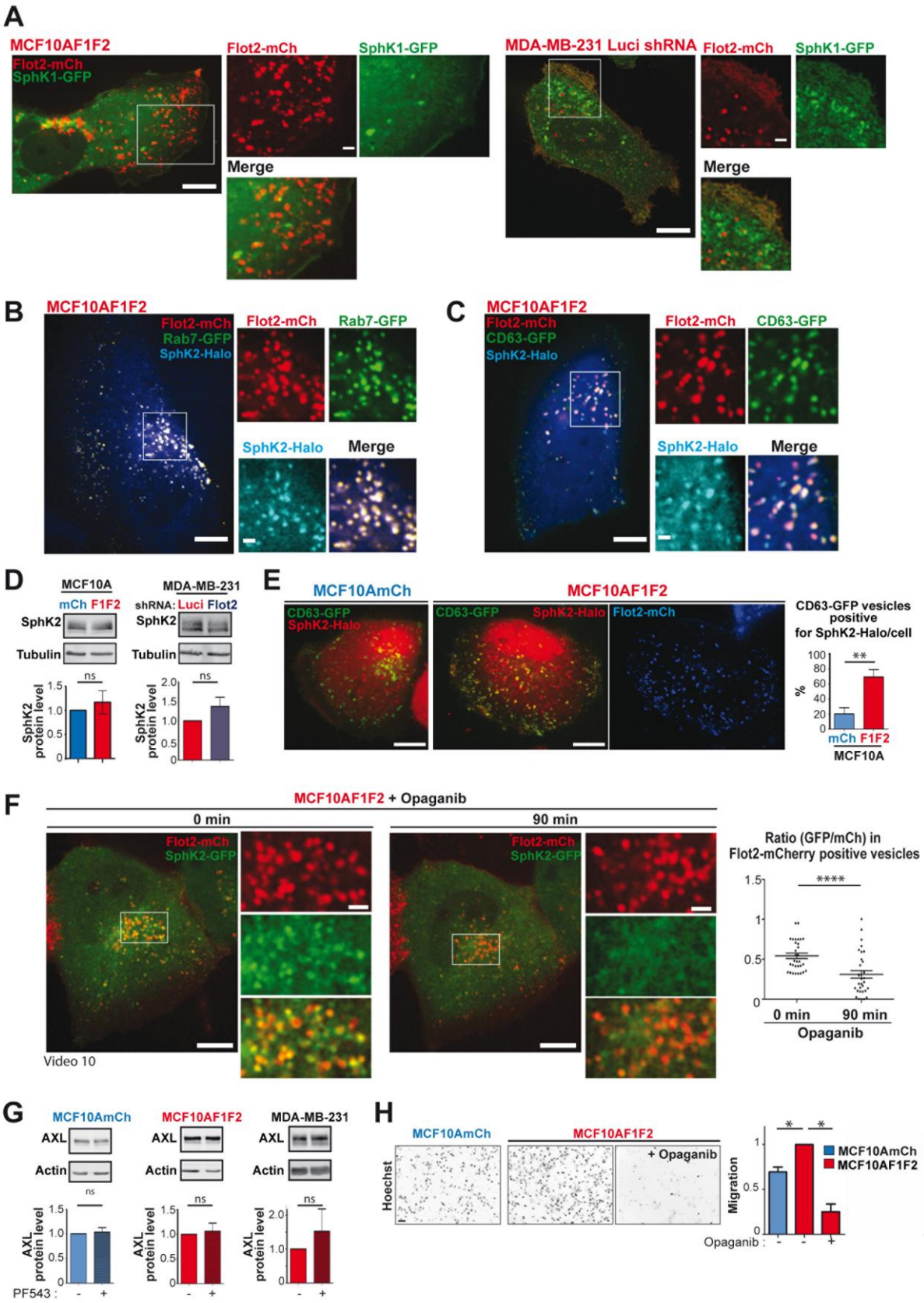
A
MCF10AF1F2
Flot2-mCh
SphK1-GFP
Flot2-mCh
SphK1-GFP
Merge
MDA-MB-231 Luci shRNA
Flot2-mCh
SphK1-GFP
Merge
B
MCF10AF1F2
Flot2-mCh
Rab7-GFP
SphK2-Halo
Flot2-mCh
Rab7-GFP
SphK2-Halo
Merge
C
MCF10AF1F2
Flot2-mCh
CD63-GFP
SphK2-Halo
Flot2-mCh
CD63-GFP
SphK2-Halo
Merge
D
MCF10A
mCh F1F2
SphK2
Tubulin
ns
SphK2 protein level
MDA-MB-231
shRNA: Luci Flot2
SphK2
Tubulin
ns
SphK2 protein level
E
MCF10AmCh
CD63-GFP
SphK2-Halo
MCF10AF1F2
CD63-GFP
SphK2-Halo
Flot2-mCh
CD63-GFP vesicles positive for SphK2-Halo/cell
**
%
mCh F1F2
MCF10A
F
MCF10AF1F2 + Opaganib
0 min
90 min
Flot2-mCh
SphK2-GFP
Video 10
Ratio (GFP/mCh) in Flot2-mCherry positive vesicles
****
0 min
90 min
Opaganib
G
MCF10AmCh
MCF10AF1F2
MDA-MB-231
AXL
Actin
ns
AXL protein level
PF543 :
H
MCF10AmCh
MCF10AF1F2
Hoechst
+ Opaganib
Migration
MCF10AmCh
MCF10AF1F2
Opaganib :

Figure S9

Figure S9: SphK1 and 2 localization and effect of SphK inhibitors.

A) *SphK1 is barely detected in flotillin-positive endosomes.* Live MCF10AF1F2 cells that express SphK1-GFP (A), and MDA-MB-231 cells that co-express flotillin 1-mCherry and SphK1-GFP (B) were imaged by spinning disk confocal microscopy (see quantification in Fig. 7 B).

B, C) *SphK2 colocalizes with flotillins in Rab7 and CD63 positive vesicles.* Still images of live MCF10AF1F2 cells that express SphK2-Halo labeled with Halo-tag-Janelia Fluor 646 and Rab7-GFP (B), or CD63-GFP (C) imaged by spinning disk confocal microscopy.

D) *Flotillin level does not modulate SphK2 protein expression.* SphK2 and tubulin expression were assessed in whole cell extracts from MCF10AmCh, MCF10AF1F2, MDA-MB-231shLuci, and MDA-MB-231shFlot2 cells by western blotting using specific antibodies. The histograms show SphK2 level (normalized to tubulin) expressed as fold-increase compared with MCF10AmCh or MDA-MB-231shLuci cells, and data are the mean ± SEM of 4 independent experiments.

E) *SphK2 localization in CD63-positive endosomes is increased in MCF10AF1F2 cells.* MCF10AmCh and MCF10A F1F2 cells were co-transfected with CD63-GFP and SphK2-Halo labeled with Halo-Tag-Janelia Fluor 646. Representative images acquired by spinning disk confocal microscopy on live cells are shown. To better visualize the co-localization of CD63-GFP and SphK2-Halo, the SphK2-Halo and flotillin 2-mCherry signals were pseudocolored in red and blue, respectively. The presence of SphK2-Halo in CD63-GFP-positive vesicles was quantified (n=372 vesicles in 10 MCF10AmCh cells, and n=455 vesicles in 10 MCF10AF1F2 cells). Results are expressed as the percentage per cell of CD63-GFP labelled vesicles positive for SphK2-Halo. Scale bar: 10 µm. ** $p<0.01$

F) *Opaganib incubation induces the delocalization of SphK2 from flotillin-positive vesicles.* Live MCF10AF1F2 cells that express SphK2-GFP were imaged after incubation with opaganib by spinning disk confocal microscopy every 15 min. The SPK2-GFP signal associated with flotillin 2-mCherry positive vesicles was clearly decreased after 90 min of incubation. The histogram shows the GFP/mCherry signal ratio in flotillin 2-mCherry vesicles at 0 and after 90 min of opaganib incubation (31 vesicles at T0 and 32 vesicles at T90 from 3 independent cells).

Scale bars: 10 µm in the main images, and 2 µm in the magnified images from the boxed area. **** $p<0.0001$

G) *SphK1 inhibition does not influence AXL level in cells in which flotillins are upregulated.* MCF10AmCh, MCF10AF1F2 and MDA-MB-231 cells were incubated with the selective Sphk1 inhibitor PF543 (10 µM, 24h). AXL and actin levels were measured by western blotting in cell lysates. The histograms show AXL level, expressed as fold-increase compared with the control condition (no PF543), and data are the mean ± SEM of 4 independent experiments.

H) *Boyden chamber migration assay.* MCF10AmCh and MCF10AF1F2 cells were seeded in the top of Boyden chamber inserts in serum-free medium, and serum-containing medium, acting as chemoattractant, was placed in the bottom well. When indicated, opaganib (50 µM) was added in the upper and lower chambers. Representative inverted-microscopy images of Hoechst-stained nuclei of cells that migrated through the pores. The histogram shows the amount of cells that migrated compared with untreated MCF10AF1F2 cells, and data are the mean ± SEM of 4 independent experiments. Scale bar: 50µm. *$p<0.05$.

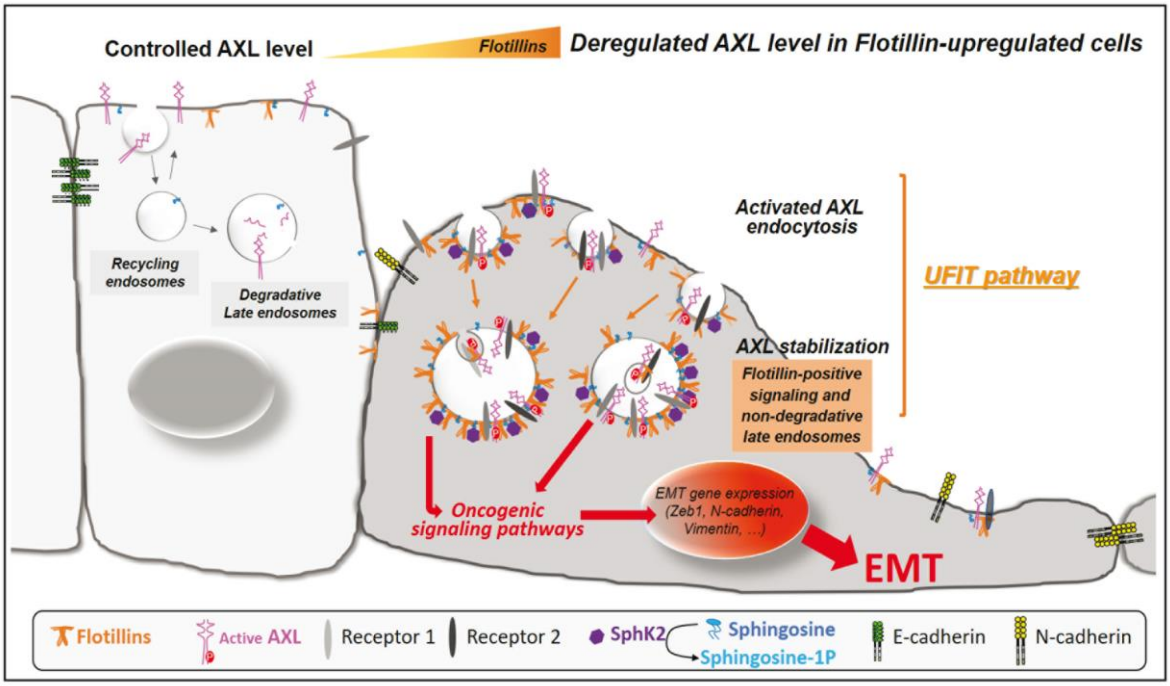

Figure 8: Model
Co-upregulation of flotillin 1 and 2 favors their oligomerization and the formation of flotillin-rich microdomains at the plasma membrane. At these membrane sites, signaling receptors, particularly the tyrosine kinase receptor AXL, are trapped. Moreover, sphingosine might be concentrated in these flotillin-rich microdomains through binding to flotillins. This promotes the recruitment of SphK2 that phosphorylates sphingosine to promote the endocytosis of AXL and other receptors in their active form. Through the UFIT pathway these receptors are delivered to "flotillin-positive late endosomes" where AXL is protected from degradation, allowing its stabilization. SphK2 is abundant in these vesicular compartments and might participate in defining their "stabilizing properties". Consequently, these flotillin-positive late endosomes act as signaling endosomes favoring the hyperactivation of oncogenic signaling pathways that promote EMT.

Discussion

In this study, we demonstrated that flotillin upregulation in non-tumoral mammary cell lines devoid of oncogenic mutations is sufficient to activate several oncogenic signaling pathways, leading to EMT induction, a key step towards cancer cell invasion. Moreover, flotillin upregulation led to the stabilization of the RTK AXL through the UFIT pathway that promotes endocytosis of several cargos from the plasma membrane toward flotillin-positive late endosomes (see model Fig. 8). The UFIT pathway is dependent on the lipid kinase SphK2, showing the role of sphingolipid metabolism on this flotillin-induced trafficking pathway. Our findings demonstrate the unprecedented role of endosomal trafficking on AXL upregulation, a major feature of several invasive tumors.

Flotillins are upregulated in many carcinoma types and also in sarcoma, and their upregulation is predictive of aggressive tumor behavior (reviewed in (*39*)). Flotillin co-upregulation is necessary and sufficient to promote breast, nasopharyngeal, and rhabdomyosarcoma cancer cell invasion (*11*, *16*, *40*), and their specific role in metastasis formation was demonstrated in flotillin 2 knock-out mice (*12*). EMT is a crucial step in tumor initiation and cancer cell dissemination, but flotillin contribution to this process remained to be addressed (*10*). Previous studies were performed in cancer cell lines with mutations in both signaling and structural genes that promote EMT induction and invasion. This did not allow determining the exact contribution of flotillin upregulation to this crucial process and the molecular mechanisms specifically deregulated. To overcome this problem, we co-upregulated flotillins 1 and 2 (same level as observed in tumors) in immortalized non-tumoral mammary cell lines (MCF10A and NMuMG) that physiologically display low flotillin expression level. In these cells, flotillin upregulation was sufficient to promote EMT through the deregulation of several PM receptors involved in the activation of key signaling pathways of EMT induction. An unbiased search of the receptors activated upon flotillin upregulation in mammary cells identified the TGF-β receptor and several RTKs, such as AXL and EphA4, implicated in mammary tumor

development (*5*, *41–43*). Flotillin upregulation in MCF10A cells led also to the activation of the Ras, ERK/MAPK, PI3-K/AKT, STAT3, Smad3 signaling pathways, but not NF-kB and WNT. Following flotillin upregulation, K-Ras and PI3K and the downstream signaling pathways, which are frequently activated in several cancers (*44*), were activated in MCF10A cells, which do not harbor mutations in these cancer driver genes (*45*). Moreover, flotillin upregulation mimics oncogenic Ras activation that is reported in MCF10A mammary cells to be correlated with ΔNp63α downregulation, PI3-K/AKT activation and ZEB1/2-mediated EMT (*25*). These findings show that flotillin upregulation mimics the effects of cancer driver gene mutations (i.e. the activation of their downstream oncogenic signaling pathways) and acts as an EMT driver. Thus, quantification of flotillin expression level in tumors, even in the absence of cancer driver gene mutations, may help in therapeutic decision-making. Moreover, as flotillin upregulation leads to the activation of several membrane receptors and oncogenic signaling pathways, limiting their function (e.g. by inhibiting their oligomerization) could allow the simultaneously targeting of several drivers of tumor cell invasion.

We demonstrated that flotillin upregulation deregulates the trafficking of plasma membrane receptors, and identified them as new cargos of the UFIT pathway. This endocytic pathway occurs in the context of flotillin upregulation, and the proteins located in the flotillin-containing PM microdomains, that could be different from one cell type to another, are endocytosed and delivered to flotillin-positive non-degradative late endosomes (*16*). In addition to their weak degradative activity, we demonstrated that these vesicles have characteristics of signaling endosomes because they contained activated RTKs. In flotillin-positive late endosomes, we also detected the cancer driver K-Ras4B, associated with increased Ras activity upon flotillin upregulation. It was previously reported that K-Ras and activated ERK1/2 are specifically recruited to Rab7-positive endosomes (*46*). Endosomes act as signaling platforms to facilitate the multiplexing of signaling molecules that in turn can affect the endosomal system by

modifying the number, size and position of endosomes, and ultimately the trafficking of such signaling molecules (*7*, *47*). In this context, the UFIT pathway is a key player to connect deregulation of endocytosis and signaling in cancer cells.

We found that AXL, as a cargo of the UFIT pathway, is maintained activated in flotillin-positive vesicles. The finding that AXL inhibition impairs flotillin-induced EMT shows its central role in this program, at least in MCF10A cells. AXL is broadly expressed in a variety of solid cancers, particularly breast carcinoma, where its level is associated with high risk of metastases and poor patient prognosis (*5*, *48*). AXL expression is correlated with the acquisition of a mesenchymal cell phenotype, invasive properties, and resistance to treatments. AXL is an attractive therapeutic target, and several AXL inhibitors are currently in preclinical and clinical development (*4*, *49–51*). Although AXL overexpression in tumors is attributed to post-transcriptional regulation, the underlying mechanisms are totally unknown. When overexpressed, AXL activation is ligand-independent and is the result of its oligomerization and/or association with other RTKs (*52*). In this context, flotillin upregulation emerges as a key process in AXL regulation. Indeed, using an optogenetic system to force flotillin oligomerization upon illumination and TIRF microscopy, we demonstrated that AXL is trapped in light-induced flotillin clusters at the PM. Moreover, flotillin/AXL clusters are co-endocytosed, and the UFIT pathway allows AXL delivery to flotillin-positive endosomes where we detected activated AXL. Thus, the UFIT pathway is crucial to sustain EMT-promoting signaling. This flotillin/AXL link is also observed in invasive breast tumor cells where flotillin 1 expression is correlated with that of AXL (Fig. S8). These discoveries open a new interesting perspective for cancer therapy. Indeed, as AXL participates in the crosstalk with other RTKs (EGFR, Met,…), its inhibition could be more effective than just EGFR inhibition because it might restore sensitivity to multiple therapies (*31*, *53*). Anti-AXL antibodies gave promising results in preclinical models of pancreatic and breast tumors (*49*, *50*, *54*). Endocytosis is

dysregulated in human tumors and its inhibition increases the availability of therapeutic monoclonal antibody targets and promotes antibody-dependent cellular cytotoxicity (*55*, *56*). Inhibition of flotillin function might have a strong effect on the efficacy of anti-AXL and also anti-RTK antibodies (e.g. the anti-EGFR antibody cetuximab) by increasing the membrane receptor availability at the cell surface, particularly in flotillin-positive tumors.

Flotillin upregulation-induced AXL stabilization requires the activity of SphK2, a lipid enzyme that maintains the cellular sphingolipid homeostasis, and a recognized target for cancer therapies (*57*, *58*). SphK2 colocalizes with flotillin-positive domains at the PM and is enriched in flotillin-positive endosomes, in agreement with previous findings showing SphK2 localization in multivesicular endosomes in K562 leukemia cells (*59*). Flotillin binding to sphingosine and ectopic flotillin overexpression allow the formation of sphingosine domains that could favor SphK2 recruitment (*33*). We found that SphK2 inhibition or knock down, in cells with upregulated flotillins, strongly reduced AXL expression level and decreased cell invasion (Fig. S9H). Conversely, SphK2 inhibition did not affect AXL level in control MCF10A or in MDA-MB-231 invasive breast cells in which flotillins were knocked down. In these cells, AXL accumulated at the PM, suggesting that the UFIT pathway targets AXL to flotillin-positive endosomes to promote its escape from mechanisms of downregulation. SphKs catalyze S1P production from sphingosine and there is a strong causal association between overactive SphK, S1P generation and cancer (*60*). SphK2 is involved in migration of MDA-MB-453 cells toward epidermal growth factor (*61*). SphK2 increase promotes oncogenesis and results from a phase 1 clinical trial supported the use of SphK2 inhibitors in cancer treatment (*57*, *58*). Showing that SphK2 inhibition impacts on AXL will help to understand the anti-tumoral function of these inhibitors and the role of SphK2 during tumor development, that is so far unknown. The UFIT pathway does not influence SphK2 expression level (Fig. S9 F), but allows its recruitment to flotillin-positive endosomes (Fig. S9 G). Modifications in SphK

subcellular localization, defined as non-oncogenic addiction, is a common mechanism during tumorigenesis (*62*). Sphingolipids are ubiquitous membrane components that are metabolized to form signaling molecules associated with cellular activities. Additional studies are required to understand whether these sphingolipid modifications at endosomes affect endosome fusion, motion, and/or function. For example, whereas flotillin 1 directly interacts with Raf, MEK1/2 and ERK1/2 (*20*), flotillin-induced lipid modifications at late endosomes might indirectly regulate protein recruitment and/or activation. For instance, S1P allows the activation of five close G-protein coupled receptors (GPCRs), either after its release in the intercellular space or directly through the outer leaflet of the plasma membrane (*63*). This leads to the subsequent induction of many downstream signaling pathways. Also, ceramide and S1P produced locally at late endosomes, again through GPCR activation, might participate in cargo sorting from the limiting late endosome membrane into their lumen (*64*, *65*).

This study adds new evidences for a crucial gain-of-function role of upregulated flotillins during EMT. We found that the UFIT pathway, by perturbing sphingolipid metabolism, allows the endocytosis of several PM receptors, particularly AXL, a major RTK during oncogenesis. AXL targeting to flotillin-positive late endosomes allows its stabilization and signaling during EMT.

Materials and methods

Cell lines

All cell lines were authenticated, tested for contamination and cultured in a 37 °C incubator with 5% CO_2. The MCF10A mammary epithelial cell line (American Type Culture Collection, ATCC CRL-10317) and the derived cell lines MCF10AmCh and MCF10AF1F2 were grown in DMEM/HAM F-12 medium supplemented with 5% horse serum (Gibco, Thermo), 10µg/ml insulin, 20ng/ml EGF, 0.5µg/ml hydrocortisone and 100ng/ml cholera toxin. The NMuMG mouse mammary epithelial cell line (ATCC CRL-1636) and the derived cell lines NMuMGmCh and NMuMG-F1F2 were grown in DMEM supplemented with 10% fetal bovine serum (FBS) (S1810-100; Biowest), 100 units/mL penicillin, 100 µg/mL streptomycin, 10 µg/mL insulin (I9278; Sigma–Aldrich). The human breast adenocarcinoma cell line MDA-MB-231 (ATCC HTB-26) and the derived cell lines MDA-MB-231shLuci MDA-MB-231 shFlot2 (described in (*16*)) were grown in DMEM with 10% FBS (Biowest, Eurobio). Retrovirus production in Phoenix cells (G. Nolan, Stanford, USA), infection and selection were performed as described (*66*). Cells were grown continuously in 1 µg/ml puromycin and 200µg/ml hygromycin.

The MCF10AF1F2 and NMuMGF1F2 cell lines that stably overexpress flotillin 1 and 2 were generated by double retroviral infection of two vectors encoding the chimeric proteins flotillin-2-mCherry and flotillin-1-HA (described in (*16*)) and then by selection for resistance against puromycin and hygromycin. Cells were then sorted by flow cytometry according to the mCherry fluorescence signal.

Plasmids and transfection

peGFP-N1-AXL was generated by subcloning the human AXL sequence (NM_021913.4) amplified by PCR using the primers 5'AAGCTTATGGCGTGGCGGTGCCCCAGG 3' and 5'

GAATTCCGGCACCATCCTCCTGCCCTG 3' between the *Hind*III and *Eco*RI sites in peGFP-N1. pHalo-N1-AXL was obtained by replacing GFP by the Halo-sequence in peGFP-N1-AXL between *Hind*III and *EcoR*I. To generate the pBabe-Flot2-CIBN-mCherry construct, the sequence encoding the CIBN domain was amplified by PCR using the primers 5' GAATTCTAATGAATGGAGCTATAGGAGG 3' and 5' CGGATTATATTCATGTACCGGTCACACA 3', and inserted, using the *Eco*RI and *Age*I sites, between flotillin 2 and mCherry in the pBabe-Flot2-mCherry plasmid (*16*). The peGFP-ERK2 construct was a gift from Dr H Farhan (University of Oslo, Norway). The CD63-GFP plasmid was a gift from Dr A Weaver (Vanderbilt University, Nashville, USA) (*67*). The Rab7a-GFP plasmid was described in (*16*). The pCMV3-N-Myc- human AXL (HG10279-NM) plasmid was purchased from Sino Biological. The peGFP-C1-KRas4A, peGFP-C3-KRas4B, peGFP-C3-HRas and peGFP-C3-NRas plasmids were gifts from Dr M Philips (NYU Cancer Institute, New York, USA). The phCMV3-Flot1-HA plasmid was a gift from Dr V Niggli (University of Bern, Switzerland) and pmCherry-N1-Flot2 was previously described (*16*). The plasmids encoding the different TAp63 α,β,γ and ΔNp63 α,β,γ isoforms were gifts from Dr C Caron de Fromentel (INSERM UMR590, Lyon, France) (*68*), the PCS2+chickenEphA4-GFP plasmid was a gift from Prof F Fagotto (CRBM, Montpellier, France) (*69*). The TGFβRI-GFP and TGFβRII-Flag constructs were gifts from Dr R Derynck (UCSF, San Francisco, USA) (*70*). The SphK1-GFP and SphK2-GFP constructs were gifts from Prof P de Camilli (Yale School of Medecine, New Haven, USA) (*34*). The SphK2-Halo plasmid was obtained by replacing GFP with the Halo-sequence between *Eco*RI and *Not*I. The CRY2-mCitrin plasmid was a gift from Prof W Do Heo (KAIST, Dajeon, South Korea), previously described in (*32*). The TfR(CD71)-GFP vector was purchased from Addgene. Cells were transfected with the indicated constructs using the JetPEI or JetPrime Transfection Reagents (Polyplus Transfection, Illkirch, France).

Antibodies and reagents

Mouse antibodies used were against: actin (A5441, Sigma), flotillin 1 and flotillin 2 (BD Biosciences), E-cadherin (used for MCF10A cells, Life-technologies), E-cadherin (used for NMuMG cells, BD Biosciences), LAMP1 (used for MCF10A cells, BD Biosciences), Smad3 (ThermoFisher), vimentin and α-tubulin (Sigma), phosphorylated ERK1/2 at T202/Y204 and AKT (CST), pan-Ras (Millipore), phosphorylated Y (4G10), EphA4 (gift from Dr Greenberg, Harvard, Boston, USA) (*69*), and STAT3 (CST, #9139S). Rabbit antibodies were against flotillin 1 (F1180, Sigma), flotillin 2 (3436, CST), AXL (C89E7, CST), phosphorylated AXL at Y702 (D12B2, CST), ERK1/2 (CST), phosphorylated AKT at S473, ZEB1 (Santa Cruz), ZO-1 (Zymed), phosphorylated Smad3 at S423/425, p63, and phosphorylated EphA4 at Y588/596 (Abcam), phosphorylated STAT3 at Y705 (#9131S, CST), p65-NFκB (Santa Cruz), β-catenin (Sigma, 2206), HA-tag (Invitrogen), Flag-tag (Sigma), Myc-tag (Upstate), SPK2 (Clone D2V3G, CST). The humanized anti-AXL antibody D4 (https://patents.google.com/patent/EP3229836A1/en?oq=EP3229836A1) and the mouse anti-AXL antibody D9 (*49*) were gifts from Dr B Robert (ICRM, Montpellier, France). Alexa-488, -546, -633 -conjugated secondary antibodies were from Thermo Scientific. Alexa-Fluor-488-phalloidin was from Invitrogen and Hoechst (0.1 mg/ml) was from Sigma-Aldrich. LPS (Sigma, L5668) was used at 1µg/ml for 1h. Halo-tagged proteins were labeled by incubating cells with 200nM HaloTag Ligand conjugated to Janelia Fluor 646 (Promega) for 30 min before imaging. Opaganib (ABC294640) (used at 50 µM up to 10 hours) and PF543 (used at 10 µM up to 24h) were from Selleckchem. Cycloheximide (used at 100 µg/ml for 6h) was from Sigma-Aldrich.

RNA interference

The pSIREN-RetroQ-Flot2-shRNA (targeting both human and murine Flot2) and pSIREN-RetroQ-Luciferase shRNA vectors were previously described (*71*). Luciferase shRNA (shLuci)

was used as control (*66*). For RNA-mediated interference experiments, cells were transfected using Interferin (Polyplus Transfection) with siRNA oligonucleotide duplexes (Eurogentec, Belgium). The sequences of the siRNA duplexes were: for human ZEB1, 5' GGUAGAUGGUAAUGUAAUA 3' matching with the human ZEB1 sequence (NM_001128128.2) previously used in (*72*); for human ZEB2 5' GCAUGUAUGCAUGUGACUU 3' matching with the human ZEB2 sequence (NM_014795.3) previously used in (*73*); for human AXL 5' CGAAAUCCUCUAUGUCAACAU 3' matching with the human AXL sequence (NM_021913.4) and previously used in (*74*); for control siRNA (Eurogentec, SR-CL000-005); for human SphK2 5' GCUGGGCUGUCCUUCAACCU 3' matching with the human SphK2 (NM_020126.4) and previously used in (*61*).

Gel electrophoresis and immunoblotting

Protein concentrations in whole-cell lysates were determined with the BCA protein assay kit (Pierce). Proteins from whole cell lysates (20–60 µg) were separated on 8-10-12% polyacrylamide gels and transferred to Immobilon-FL membranes (Millipore). Primary and secondary antibodies were diluted in blocking buffer (Millipore) containing 0.1% Tween 20. Detection and analysis were performed using the Odyssey Infrared imaging system (LI-COR Biosciences). Immunoblots were quantified by densitometry using Odyssey V3.0 and Fiji.

Immunoprecipitation

The rabbit polyclonal anti-AXL (CST, 8661) antibody (1µg) was incubated with Dynabeads (25 µl) Protein G at room temperature for 1h. Antibody coated-beads were then incubated with 1 mg of proteins from post-nuclear supernatants of the indicated cells at 4°C for 2 h, washed and loaded on SDS-PAGE. Immunoprecipitates were analyzed by western blotting.

Phospho-RTK and phospho-kinase arrays

The Proteome Profiler Human Phospho-RTK array kit and human phospho-kinase antibody array kit (R&D Systems) were used according to the manufacturer's instructions. Both array types were incubated with 200 µg of proteins from post-nuclear supernatants isolated from each tested cell line maintained for 48h (human-phosphokinase array) or 24h (human phospho-RTK array) in complete culture medium after seeding.

Measurement of Ras activity

Cells were lysed in lysis buffer A (50 mM Tris pH 7.5, 10 mM $MgCl_2$, 0.3 M NaCl, 2% (v/v) IGEPAL). Lysates were then incubated with 30 µg of Ras-GTP Binding Domain (RBD of human c-Raf kinase) fused with GST associated to beads (#RF02, Cytoskeleton) at 4°C for 1h. Prior to incubation with beads, 1/20 of each cell lysate was collected to be used as "input". Precipitates and inputs were revealed by western blotting using an anti-pan-Ras antibody.

AXL uptake assays

Cells were seeded in 12 mm sterile poly-lysine-coated round glass coverslips and grown to 60-70% confluence. After 15 min incubation at 4°C in serum-free medium, cells were incubated at 4°C in serum-free medium containing 250 µg/ml of D4 anti-AXL humanized antibody for 45 min. Alternatively, cells transfected with the plasmid encoding N-terminally Myc-tagged AXL (N-Myc-AXL) were incubated with the anti-Myc (9E10) antibody. Cells were extensively washed with cold serum-free medium to remove unbound antibodies and surface-bound antibodies were internalized by incubating cells at 37°C in serum-free medium for the indicated time points. Cells were then fixed and permeabilized, and the internalized primary antibody molecules were detected using the appropriate fluorescent secondary antibody (FITC-

conjugated anti-human IgG for cells incubated with the D4 antibody, and Alexa488- conjugated anti-mouse IgG for cells that express N-Myc-AXL). Samples were then processed as described in the Immunofluorescence and image acquisition chapter.

Surface biotinylation assays/internalization experiments

Cells were seeded and after 24 hours were washed with chilled PBS, incubated with biotin NHS (0.2mg/ml in PBS pH 7.9) at 4°C for 45 min, and shifted to 37°C for the indicated times. Cells were then incubated with Mesna buffer at 4°C for 15 min to remove the remaining cell-surface biotin, followed by a 10min incubation at 4°C with iodoacetamide to stop the action of Mesna. Cells were then scraped in lysis buffer (10 mM Pipes pH 7, 100 mM NaCl, 300 mM sucrose, 3 mM $MgCl_2$, 0.5% (v/v) IGEPAL CA-640, 1 mM EDTA, 1 mM Na_3VO_4, protease inhibitor cocktail) and the postnuclear supernatants were harvested after centrifugation (10.000rpm 4°C for 10 min). One cell plate was lysed right after biotinylation and before incubation with Mesna buffer and used to estimate the amount of total labeled surface proteins. An equal protein amount for each time point was incubated with streptavidin-coated agarose beads (at 4°C for 45 min). After two washes in PBS, beads were precipitated and resuspended in Laemmli buffer. Samples were separated by SDS-PAGE followed by western blotting with antibodies against AXL and CD71.

Results from the experiment performed using MCF10AmCh and MCF10AF1F2 cells were not expressed as the percentage of total surface labelled AXL at T0min because the total amount of AXL in MCF10AF1F2 cells was higher than in MCF10Amch cells (see panel G of Figure 6). To estimate correctly the internalization rate, results at each time point were expressed as the percentage of the maximum level of internalized protein. Because the global level of AXL remained unchanged between MDA-MB-231shLuci and MDA-MB-231shFlot2 cells, results

for each time point were expressed as the percentage of the maximum level of surface labeled AXL or CD71 at T0min.

Immunofluorescence and image acquisition

Cells were fixed in 3.2% paraformaldehyde (PFA) for 10 min, followed by a 2min permeabilization with 0.1% Triton X-100 or by a 10min permeabilization with 0.05% saponin, and a 15min saturation in the presence of 2% BSA. Cells were then incubated with primary and secondary antibodies. For CD63, LAMP1, and flotillin immunostaining, cells were fixed and permeabilized with acetone/methanol (v/v, 1/1) at -20°C for 2 min. Images were taken with a confocal SP5-SMD microscope (Leica) with 40×/1.3 or 63×/1.4 oil HCX PL APO CS objectives (Leica), and captured with a hybrid detector (Leica HyD) controlled using the C software. Images were analyzed with the Fiji software. In some cases, stacks of confocal images with a step size of 0.3µm were processed with Imaris (Bitplane, Zurich, Switzerland) for visualization and volume rendering. Images were processed using Adobe Photoshop and assembled using Adobe Illustrator.

Quantification of AXL surface staining

Fixed non-permeabilized cells were immunostained for AXL using the monoclonal D4 antibody against AXL extracellular domain and an Alexa 488-conjugated anti-human secondary antibody. Images were acquired by confocal microscopy under the same illuminated conditions. Using the Fiji software, the outline of each cell was defined and the mean fluorescence intensity (taking into account the cell surface) was quantified in the area defined by the outline.

Optogenetic and TIRF microscopy

MCF10A cells were co-transfected with vectors encoding CRY2-mCitrin, flotillin 2-CIBN-mCherry and AXL-Halo labeled with the Halo-Tag-Ligand-Janelia Fluor 646. TIRF images were acquired using an inverted Nikon microscope and a 100×/1.49 oil objective controlled using the Metamorph software (1 image /s). First, Flot2-CIBN-mCherry and AXL-Halo were imaged for 10 seconds before 488nm illumination. Then, cells were globally illuminated by 22 pulses (1 pulse/s, 100 ms time length for each pulse) of 488nm-light and simultaneously CRY2-mCitrin, Flot2-CIBN-mCherry and AXL-Halo signals were imaged for 3 min.

Quantification of SphK2-GFP delocalization from flotillin-positive late endosomes

MCF10AF1F2 cells that express SphK2-GFP were imaged by spinning disk confocal microscopy (1 image/15 min). The Fiji software and images acquired at 0 and 90 min after opaganib (50µM) addition in the culture medium were used to define same-size individual regions of interest (ROI) surrounding one flotillin 2-mCherry-positive vesicle. For each ROI, the mean intensity corresponding to the mCherry and the GFP signals was quantified. To take into account the decrease in signal intensity due to photobleaching, quantifications were done also on three ROI of the same size, but outside flotillin 2-mCherry-positive vesicles. The mean of the obtained values was considered as background and subtracted from the GFP and mCherry signals measured in the ROI surrounding vesicles. Then, the GFP/mCherry signal ratio was individually calculated for each ROI surrounding a vesicle on images acquired at 0 and 90 min after opaganib addition.

Time-lapse imaging experiments

Time-lapse imaging experiments were performed using an inverted Spinning disc Nikon Ti Andor CSU-X1 microscope equipped with a focus Fluor 100 × objective (NA 0.55). Time-

series images were acquired with a EMCCD iXon897 Andor camera controlled by the Andor iQ3 software. Time lapse was started 24/48h after transfection. Time series of the captured images were saved as .tiff files that were compiled into .avi movies using the Fiji software.

Scanning electron microscopy

PBS-washed cells were fixed with 2.5% glutaraldehyde in PHEM buffer, pH 7.2 at room temperature for 1 hour, and then washed in PHEM buffer. Fixed cells were dehydrated using a graded ethanol series (30-100%), followed by 10 min in graded ethanol-hexamethyldisilazane and 10 min in hexamethyldisilazane. Then, samples were sputter coated with a 10nm thick gold film and examined using a scanning electron microscope (Hitachi S4000, at CoMET, MRI-RIO Imaging, Biocampus, INM Montpellier France) and a lens detector with an acceleration voltage of 10KV at calibrated magnifications.

RNA isolation and sequencing

Total RNA was prepared from MCF10AmCh and MCF10AF1F2 cells using the RNeasy Mini Kit (Qiagen) according to the manufacturer's instructions. RNA quantity and quality were determined with an Agilent RNA 600 Nano Bioanalyser (Agilent Technologies), and total RNA was concentrated to 100 ng/µl. Pure RNA preparations without DNA or protein contamination were used for sequencing. Libraries, processed by Fasteris SA (Geneva, Switzerland), were prepared with the TruSeq Stranded mRNA Library Prep Kit from Illumina. Fragments were sequenced on an Illumina Hi-Seq 4000 sequencer according to the manufacturer’s instructions.

Differential analysis of transcriptomic data

The differential gene expression analysis was carried out using three replicates per condition to compare the transcript levels between MCF10AmCh and MCF10AF1F2 cells. Two analysis

methods were used: DESeq (http://bioconductor. org/packages/release/bioc/html/DESeq.html) and Tuxedo (http://cufflinks.cbcb.umd.edu/).

Genes with a p_{adj} <0.05 were assigned as differentially expressed. The Deseq2 and Tuxedo results were compared. Only genes with an expression fold change >2.8 were considered. Using this criterion 802 up- and down-regulated genes were identified.

Gene functional classification: GO term enrichment analysis

The PANTHER (protein annotation through evolutionary relationship, version 13.1) classification system (http://www.pantherdb.org/) was used to perform a Gene-Ontology (GO) enrichment. Enriched terms were considered statistically significant when p_{adj} was <0.05, and a minimum of five genes were grouped for each significant term. GO terms were categorized in three major functional groups: biological process, molecular function, and cellular component.

Reverse Transcription-quantitative real-time PCR (RT-qPCR)

RNA was extracted from the indicated cell lines as described above. Then, mRNA samples were reverse transcribed to cDNA using SuperScript II Reverse Transcriptase (Thermo Fisher Scientific) and qPCR was performed using an LC480 apparatus (Roche) with the SYBR Green PCR Master Mix (Applied Biosystems). The primer sequences were: for human CDH1 forward 5' TCATGAGTGTCCCCCGGTAT 3' and reverse 5' CAGCCGCTTTCAGATTTTCAT 3'; for human CDH2, forward 5' GGCAGAAGAGAGACTGGGTC 3' and reverse 5' GAGGCTGGTCAGCTCCTGGC 3'; for human vimentin, Duplex QT00095795 (Quiagen); for human ZEB1, forward 5' GCACCTGAAGAGGACCAGAG 3' and reverse 5' TGCATCTGGTGTTCCATTTT 3'; for human ZEB2, forward 5' GGGAGAATTGCTTGATGGAGC 3' and reverse 5' TCTCGCCCGAGTGAAGCCTT 3'; for

human MRPL19 (internal control), forward 5' GGGATTTGCATTCAGAGATCAG 3' and reverse 5' GGAAGGGCATCTCGTAAG 3'; for murine CDH1, forward 5' GGTCTCTTGTCCCCACA 3' and reverse 5' CCTGACCCACACCAAAGTCT 3'; for murine CDH2, forward 5' AGGGTGGACGTCATTGTAGC 3' and reverse 5' CTGTTGGGGTCTGTCAGGAT 3'; for murine vimentin, forward 5' AATGCTTCTCTGGCACGTCT 3' and reverse 5' GCTCCTGGATCTCTTCATCG 3'; for murine ZEB1, forward 5' GCTCAGCCAGGAACCCGCAG 3' and reverse 5' TGGGCACCCTCTGCCACACA 3'; for murine ZEB2, forward 5' ATGGCAACACATGGGTTTAGTGGC 3' and reverse 5' ATTGGACTCTGAGCAGATGGGTGT 3'; for murine MmRPL32 (internal control), forward 5' TTAAGCGAAACTGGCGGAAAC 3' and reverse 5' TTGTTGCTCCCATAACCGATG 3'; for human AXL, forward 5' GTGGGCAACCCAGGGAATATC 3' and reverse 5' GTACTGTCCCGTGTCGGAAAG 3'.

RT-qPCR analysis of breast tumor samples

The mRNA levels of flotillin 1 and ΔNp63 in tumor samples from the cohort of patients with breast cancer were analyzed as described (*75*).

Boyden chamber migration assay

Cells ($5x10^4$) were seeded on the upper chamber of the Boyden chamber inserts (Corning FluoroBlok cell culture insert, 8 µm pores) in 250µl of DMEM/F12 with 1% horse serum. In the lower chamber, complete medium (750µl) was added, as chemoattractant. Opaganib (50 µM) or PF543 (10 µM) was added in the upper and lower chambers. After 14h, cells at the bottom of the filter were fixed with 3.2% paraformaldehyde and stained with Hoechst. The nucleus of cells that had migrated through the pores was imaged with an

EVOS microscope (Life technologies) using a 10x objective. Semi-automatic quantification was performed with Fiji. For each experiment, each condition was performed in triplicate.

Patients and specimens

Patients (n=9) with invasive breast carcinoma were treated at the Cancer Research Institute, Tomsk NRMC (Tomsk, Russia). Frozen and Formalin-fixed paraffin-embedded (FFPE) tumor tissue specimens obtained during surgery were used for immunofluorescence analyses.

The histological type was defined according to the World Health Organization recommendations (*76*). Tumor grade was determined using the Bloom and Richardson grading system (*77*). The expression of estrogen receptor (ER) and progesterone receptor (PR) was scored using the HSCORE method (*78*). HER2 expression was analyzed by immunohistochemistry and calculated on a scale 0-3+, according to the ASCO/CAP guidelines (*79*). Ki-67 expression was calculated as the percentage of Ki-67-positive tumor cells relative to all tumor cells. Molecular subtypes were categorized on the basis of the primary tumor ER, PR, HER2, and Ki-67 status, according to the St Gallen recommendations (*79*). luminal A (ER^+ and/or PR^+, $HER2^-$, and Ki-67 <20%), luminal B (ER^+ and/or PR^+, $HER2^{+/-}$, and Ki-67 ≥20%), $HER2^+$ (ER^- and PR^-, $HER2^+$), and triple-negative (ER^-, PR^-, $HER2^-$). The study procedures were in accordance with the Helsinki Declaration (1964, amended in 1975 and 1983). This study was approved by the institutional review board; all patients signed an informed consent for voluntary participation.

Immunofluorescence staining on patient tumor samples

Seven µm-thick FFPE tumor sections were deparaffinized, rehydrated, processed for heat-induced epitope retrieval with EDTA buffer (pH 8.0) using PT Link (Dako, Denmark), and blocked with 3% bovine serum albumin (Amresco, USA) in PBS. Expression of flotillin 1 (F1180, 1:50, Sigma) and AXL (C89E7, CST), was assessed using the BondRXm

immunostainer (Leica, Germany). TSA visualization was performed with the Opal 520 and Opal 690 (Opal seven-color IHC Kit (NEL797B001KT; PerkinElmer), nuclei stained with DAPI and samples mounted in Fluorescence Mounting Medium (Dako, Denmark). Samples were analyzed using the Vectra 3.0 Automated Quantitative Pathology Imaging System (PerkinElmer, USA).

Zebrafish strains.

The zebrafish (*Danio rerio*) Tg(FoxD3::GFP) and Tg(Fli1::GFP) lines were maintained under standard laboratory conditions according to the European Union guidelines for the handling of laboratory animals (http://ec.europa.eu/environment/chemicals/lab_animals/home_en.htm), and experiments were approved by the Direction Sanitaire et Vétérinaire de l'Hérault and Comité d'Ethique pour l'Expérimentation Animale under reference B-34-172-39 and CEEA-LR-13007.

Flotillin 2 morpholino design and microinjection

Morpholino targeting the ATG region of flotillin 2 mRNA and the standard control oligonucleotide (Gene Tools Inc.) were previously described (*23*). They were injected in 1-cell embryos (4 ng and 10 nm for MoATGFlot2 and MoCtrl, respectively). After incubation at 28°C, embryos were examined at the 20-somites stage.

Immunohistochemistry of zebrafish embryos

At the 20-somite stage, injected embryos were fixed in 4% paraformaldehyde in phosphate-buffered saline (PBS) at 4°C overnight. Manually dechorionated embryos were permeabilized in 0.1% Triton X-100 in PBS under gentle shaking. Embryos were blocked with 5% BSA, 1% goat serum in PBS/0.1% Triton X-100 at room temperature for 4h. Embryos were then incubated with a mouse primary antibody against flotillin 2 (BD Biosciences) at 4°C overnight. Embryos were washed in PBS/0.1% Triton X-100 and incubated with an Alexa Fluor 546-

conjugated secondary antibody (2h), then with 0.01% Hoechst 33342 (15 min), and washed. Then, embryos were embedded in agar-sucrose solution (1.5% agar, 5% sucrose) at 4°C overnight, 12 µm-thick sections were cut using a Leica VT1000S vibratome, and mounted on glass coverslips. Images were taken using a confocal Leica SP5-SMD microscope and LEICA 40x/1.3 and 63x/1.4 OIL HCX PL APO CS objectives. Images were treated with the ImageJ software (National Institutes of Health).

Time-lapse imaging, measurements of cell velocity, persistence and directionality

Once injected with MoCtrl or MoATGFlot2 morpholinos, Tg(FoxD3::GFP) 20-somite stage embryos were imaged using a Leica SP5-SMD microscope equipped with a motorized stage and a heated-regulated-incubator at 28°C. Images were taken every 2 min for 2 hours, using a LEICA 63x/1.4 OIL HCX PL APO CS objective, focusing on groups of cranial neural crest cells at the dorsal side of the neural tube, before delamination. Stacks of at least 10 planes with a Z step of 1 µm were taken for each time point. A manual tracking plugin from the ImageJ software was used to record the "x/y" position of each cell at each time point. Cell migration parameters were calculated using the Ibidi Chemotaxis tool (http://ibidi.com/software/chemotaxis_and_migration_tool/) and extracted for statistical analysis.

Morphological analysis of NCC tissue derivatives

Tg(Fli1::GFP) embryos injected with MoCtrl and MoATGFlot2 were maintained until larval stages (4 days post-fertilization). Larvae were anesthetized using 0.001% tricaine and mounted in ventral and lateral orientation for image acquisition with a Leica SP5 SMD microscope and a 10x/0.3 HCX PL objective. Focusing on the jaws and the branchial arches, 20 images were acquired (Z step of 2 µm). Z projection of all the planes were obtained and the jaw angle was determined using ImageJ. The angle values for each group were extracted for statistical analysis.

Statistical analysis

All statistical analyses were performed using SPSS version 22, and graphs were generated with Prism GraphPad version 5. All data were first tested for normality using the Kolmogorov–Smirnov normality test. For experiments with n >30, the Student's *t* test was used to identify significant differences between experimental conditions. For experiments with n <30, the non-parametric Mann-Whitney U test was used. The n value and number of independent experiments are listed in the figure legends. At least three independent experiments were performed. In the figures, the differences are significant only when indicated.

Aknowledgements

We thank Peggy Raynaud, Dominique Helmlinger and Dylane Detilleux for help in the transcriptomic analysis. We acknowledge Virginie Georget, Chantal Cazevieille, Orestis Faklaris, Sylvain de Rossi and Volker Baeker from the Montpellier Imaging Facility MRI, member of the national infrastructure France-BioImaging infrastructure.

The authors declare no competing financial interests

Funding

This work was supported by the “Fondation pour la Recherche Médicale” (DEQ20161136700). Montpellier Imaging Facility is supported by the French National Research Agency (ANR-10-INBS-04, “Investments for the future”. Collection of breast tumour samples was supported by the Russian Science Foundation (grant 19-75-30016). C.G.R. was supported by Institut National de la Santé et de la Recherche Médicale, M.G by the french ministry for scientific research and S.B by the University of Montpellier.

Supplementary Data

Supplementary information regarding patient tumor samples

Clinicopathological characteristics of the patients who gave the breast cancer samples used for this expression analysis:

Triple negative subtype: Patient #1: 65-year-old woman, invasive carcinoma (left side), T2N1M0, grade 3, ER−, PR−, Her2−, Ki-67-positive cells (50%), triple-negative. Lymph node-positive (1 metastasis from 6 lymph nodes).Five courses of neoadjuvant chemotherapy. Patient #2: 55-year-old woman, invasive carcinoma (left side), T1N0M1, multifocal, grade 2, ER^-, PR^-, $Her2^-$, Ki-67-positive cells (31%), triple-negative. Lymph node negative (0 metastasis in 7 lymph nodes).Six courses of neoadjuvant chemotherapy. Patient #3: 55-year-old woman, invasive carcinoma (left side), T2N1M0, grade 2, ER-, PR-,$Her2^-$,Ki-67-positive cells (31%). Lymph node negative (0 metastasis in 7 lymph nodes). Six courses of neoadjuvant chemotherapy.

Luminal subtype: Patient #1: 49-year-old woman, invasive carcinoma (right side), T2N0M0, grade 2, ER+, PR+,$Her2^-$,Ki-67-positive cells (10%). Lymph node negative (0 metastasis in 3 lymph nodes). No neoadjuvant chemotherapy. Patient #2: 66-year-old woman, invasive carcinoma (right side), T2N1M0, grade 2, ER+, PR+,$Her2^-$,Ki-67-positive cells (35%). Lymph node positive (3 lymph nodes with mts from 10 lymph nodes). No neoadjuvant chemotherapy. Patient #3: 40-year-old woman, invasive carcinoma (right side), T2N1M0, grade 2, ER+, PR+,$Her2^-$,Ki-67-positive cells (33%). Lymph node positive (2 lymph nodes with mts from 10 lymph nodes). No neoadjuvant chemotherapy.

HER2 subtype: Patient #1: 47-year-old woman, invasive carcinoma (right side), multifocal, T4N2aM0, grade 3, ER-, PR-,$Her2^+$,Ki-67-positive cells (65%). Lymph node positive (7 lymph nodes with mts from 16 lymph nodes). Six courses of neoadjuvant chemotherapy. Patient #2: 46-year-old woman, invasive carcinoma (right side), T2N0M0, grade 2, ER-, PR-,$Her2^+$,Ki-67-positive cells (53%). Lymph node negative (0 metastasis in 7 lymph nodes). One course of neoadjuvant chemotherapy. Patient #3: 52-year-old woman, invasive carcinoma (left side), T2N1M0, grade 2, ER-, PR-,$Her2^+$,Ki-67-positive cells (42%). Lymph node positive (6 lymph nodes with mts from 8 lymph nodes). No neoadjuvant chemotherapy. Distant metastasis in liver and lung.

Supplementary Tables

Table S1: List of the 802 genes (232 upregulated and 570 downregulated genes) that were found to be differentially expressed between MCF10AmCh- and MCF10AF1F2 cells (fold change: 2.8, $P<0.05$) using the Deseq2 and Tuxedo pipelines. This analysis was performed using three replicates per condition to compare transcripts levels between MCF10AmCh and MCF10AF1F2 cells.

Table S2: List of the enriched GO terms and the enriched pathways obtained from the analysis of the 802 differentially expressed genes between MCF10mCh and MCF10AF1F2 cells using three distinct bioinfomatic tools (KEGG, DAVID, and Genomatix). Only the data with p value <0.001 were retained.

Supplementary videos legends

Video 1: *Flotillin 2 and AXL colocalize in intracellular vesicles.* MCF10AF1F2 cells that co-express flotillin 1-HA, flotillin 2-mCherry and AXL-GFP were imaged by spinning disk confocal microscopy; 1 frame/1.3 s. Scale bar: 5 µm.

Video 2: *Flotillin 2 and AXL colocalize in intracellular vesicles in tumor cells.* One MDA-MBA-MB-231 cell that co-expresses flotillin1-HA, flotillin-2-Cherry and AXL-GFP was imaged by spinning disk confocal microscopy; 1 frame/0.8 s. Bar: Scale bar: 10µm.

Video 3: *Flotillin 2 and Kras4B colocalize in intracellular vesicles.* MCF10AF1F2 cells that express Kras4B-GFP were imaged by spinning disk confocal microscopy; 1 frame /0.8 s. Scale bar: 10 µm.

Video 4: *Flotillin oligomerization induced by a CRY2-CIBN-based optogenetic approach promotes AXL co-clustering*. Movie of the boxed area from Figure 6 D. MCF10A cells that co-

express CRY2-mCitrin (green), flotillin 2-CIBN-mCherry (red) and AXL-Halo (blue) labeled with Halo-Tag-Janelia Fluor 646 were imaged by TIRF microscopy. First, flotillin 2-CIBN-mCherry and AXL-Halo were imaged for 8 seconds before 488nm illumination. Then, cells were globally illuminated by 20 pulses (1 pulse/s, 100 ms time length for each) of 488nm-light to stimulate and visualize CRY2. During and after illumination, flotillin 2-CIBN-mCherry and AXL-Halo were continuously imaged. Two examples of flotillin 2/AXL-positive clusters induced by CRY2 oligomerization initiated by illumination are indicated (closed arrow). Co-localization events between flotillin 2-CIBN-mCherry and AXL-Halo are also visible independently of CRY2 oligomerization before illumination and correspond mostly to AXL-containing vesicles positive for flotillin 2 passing through the 200 nm depth of field illuminated by TIRF. Thanks to the high concentration of flotillin 2-CIBN-mCh in these vesicles, CRY2 translocation could be observed. Scale bar: 2 µm.

Video 5: *Co-endocytosis of flotillin 2 and AXL after their co-accumulation at the plasma membrane.* MCF10AF1F2 cells that co-express flotillin 1-HA, flotillin 2-mCherry and AXL-GFP were imaged by spinning disk confocal microscopy (1 frame/1.3 s. Scale bar: 2.5 µm). Arrows indicate the site of co-accumulation of AXL and flotillin 2 and then the emerging endocytic vesicle.

Video 6: *SphK2 is abundant in flotillin-positive late endosomes in MDA-MB-231 cells.* Movie of the boxed area shown in Figure 7 B acquired by spinning disk confocal microscopy of one MDA-MB231 cell that co-expresses flotillin 1-mCherry and SphK2-GFP (1 frame/s. Scale bar: 2 µm).

Video 7: *Co-localization and co-trafficking of AXL-Halo, SphK2-GFP and flotillin 2-mCherry in one MCF10AF1F2 cell.* Movie acquired by spinning disk confocal microscopy of one

MCF10AF1F2 cell that co-expresses flotillin 2-mCherry (red), SphK2-GFP (green) and AXL-Halo (blue) (labeled with Halo-tag-Janelia Fluor 646) (1 frame/10 s. Scale bar: 10 µm).

Video 8: *Flotillin 2-mCherry/SphK2-GFP co-endocytosis in MCF10AF1F2 cells.* Movie of the boxed area shown in Figure 7 D (upper panel) acquired by spinning disk confocal microscopy of one MCF10AF1F2 cell that co-expresses flotillin 2-mCherry and SphK2-GFP (1 frame/2 s). At 34s, arrows indicate sites of flotillin 2-mCherry and SphK2-GFP co-accumulation at the plasma membrane followed by endocytosis of a vesicle positive for both proteins. (Scale bar: 2 µm).

Video 9: *Flotillin 1-mCherry/SphK2-GFP co-endocytosis in MDA-MB-231 cells.* Movie of the boxed area shown in Figure 7 D (lower panel) acquired by spinning disk confocal microscopy of one MDA-MB-231 cell that co-expresses flotillin 1-mCherry and SphK2-GFP. The arrow indicate the site of flotillin 1-mCherry and SphK2-GFP co-accumulation at the plasma membrane followed by endocytosis of one vesicle positive for both proteins (1 frame/1 s). (Scale bar: 2 µm).

Video 10: *Inhibition of SphK2 catalytic activity induces its delocalization from flotillin-positive endosomes*. One MCF10AF1F2 cell that co-expressesing SK2-GFP was imaged by spinning disk confocal microscopy immediately after addition of opaganib (50 µM) (1 frame/30 s. Scale bar: 10 µm). The disappearance of the SphK2-GFP signal in flotillin 2-mCherry-positive vesicles is clearly visible after 8 min and lasted for the rest of the movie (up to 30 min).

References

1. A. Dongre, R. A. Weinberg, New insights into the mechanisms of epithelial-mesenchymal transition and implications for cancer. *Nat. Rev. Mol. Cell Biol.* (2018), doi:10.1038/s41580-018-0080-4.

2. A. Puisieux, T. Brabletz, J. Caramel, Oncogenic roles of EMT-inducing transcription factors. *Nat. Cell Biol.* **16**, 488–494 (2014).

3. C. Zhu, Y. Wei, X. Wei, AXL receptor tyrosine kinase as a promising anti-cancer approach: Functions, molecular mechanisms and clinical applications. *Mol. Cancer*. **18** (2019), doi:10.1186/s12943-019-1090-3.

4. C. M. Gay, K. Balaji, L. A. Byers, Giving AXL the axe: Targeting AXL in human malignancy. *Br. J. Cancer*. **116**, 415–423 (2017).

5. C. Gjerdrum *et al.*, Axl is an essential epithelial-to-mesenchymal transition-induced regulator of breast cancer metastasis and patient survival. *Proc. Natl. Acad. Sci.* **107**, 1124–1129 (2010).

6. R. Dobrowolski, E. M. De Robertis, Endocytic control of growth factor signalling: multivesicular bodies as signalling organelles. *Nat Rev Mol Cell Biol*. **13**, 63–60 (2008).

7. J. E. Murphy, B. E. Padilla, B. Hasdemir, G. S. Cottrell, N. W. Bunnett, Endosomes: A legitimate platform for the signaling train. *Proc. Natl. Acad. Sci.* **106**, 17615–17622 (2009).

8. S. L. Schmid, Reciprocal regulation of signaling and endocytosis: Implications for the evolving cancer cell. *J. Cell Biol.* **216**, 2623–2632 (2017).

9. S. Pust *et al.*, Flotillins as regulators of ErbB2 levels in breast cancer. *Oncogene*. **32**, 3443–51 (2013).

10. L. Zhao *et al.*, Flotillin-2 promotes nasopharyngeal carcinoma metastasis and is necessary for the epithelial-mesenchymal transition induced by transforming growth factor-β. *Oncotarget*. **6**, 9781–93 (2015).

11. S. Cao *et al.*, Upregulation of flotillin-1 promotes invasion and metastasis by activating TGF-β signaling in nasopharyngeal carcinoma. **7**, 1–13 (2015).

12. T. Berger *et al.*, Flotillin-2 deficiency leads to reduced lung metastases in a mouse breast cancer model. *Oncogene*. **32**, 4989–94 (2013).

13. O. O. Glebov, N. A. Bright, B. J. Nichols, Flotillin-1 defines a clathrin-independent endocytic pathway in mammalian cells. *Nat Cell Biol*. **8**, 46–54 (2006).

14. M. Frick *et al.*, Coassembly of flotillins induces formation of membrane microdomains, membrane curvature, and vesicle budding. *Curr. Biol.* **17**, 1151–6 (2007).

15. T. Babuke *et al.*, Hetero-oligomerization of reggie-1/flotillin-2 and reggie-2/flotillin-1

is required for their endocytosis. *Cell. Signal.* **21**, 1287–97 (2009).

16. D. Planchon *et al.*, MT1-MMP targeting to endolysosomes is mediated by upregulation of flotillins. *J. Cell Sci.* **131**, jcs218925 (2018).

17. C. Neumann-Giesen, I. Fernow, M. Amaddii, R. Tikkanen, Role of EGF-induced tyrosine phosphorylation of reggie-1/flotillin-2 in cell spreading and signaling to the actin cytoskeleton. *J. Cell Sci.* **120**, 395–406 (2007).

18. M. F. Langhorst *et al.*, Reggies/flotillins regulate cytoskeletal remodeling during neuronal differentiation via CAP/ponsin and Rho GTPases. *Eur. J. Cell Biol.* **87**, 921–31 (2008).

19. J. F. Dermine *et al.*, Flotillin-1-enriched Lipid Raft Domains Accumulate on Maturing Phagosomes. *J. Biol. Chem.* **276**, 18507–18512 (2001).

20. M. Amaddii *et al.*, Flotillin-1/reggie-2 protein plays dual role in activation of receptor-tyrosine kinase/mitogen-activated protein kinase signaling. *J. Biol. Chem.* **287**, 7265–78 (2012).

21. C. J. Gröger, M. Grubinger, T. Waldhör, K. Vierlinger, W. Mikulits, Meta-Analysis of Gene Expression Signatures Defining the Epithelial to Mesenchymal Transition during Cancer Progression. *PLoS One*. **7**, 1–10 (2012).

22. E. Theveneau, R. Mayor, Neural crest delamination and migration: From epithelium-to-mesenchyme transition to collective cell migration. *Dev. Biol.* **366**, 34–54 (2012).

23. E. A. R. Morris *et al.*, Flotillins control zebrafish epiboly through their role in cadherin-mediated cell–cell adhesion. *Biol. Cell*. **109**, 210–221 (2017).

24. B. De Craene, G. Berx, Regulatory networks defining EMT during cancer initiation and progression. *Nat. Rev. Cancer*. **13**, 97–110 (2013).

25. K. E. Yoh *et al.*, Repression of p63 and induction of EMT by mutant Ras in mammary epithelial cells. *Proc. Natl. Acad. Sci.* **113**, E6107–E6116 (2016).

26. L. Hu *et al.*, ΔNp63α is a common inhibitory target in oncogenic PI3K/Ras/Her2-induced cell motility and tumor metastasis. *Proc. Natl. Acad. Sci.* **114**, E3964–E3973 (2017).

27. P. Gonnord, C. M. Blouin, C. Lamaze, Membrane trafficking and signaling: Two sides of the same coin. *Semin. Cell Dev. Biol.* **23**, 154–164 (2012).

28. T. Aït-Slimane, R. Galmes, G. Trugnan, M. Maurice, Basolateral Internalization of GPI-anchored Proteins Occurs via a Clathrin-independent Flotillin-dependent Pathway in Polarized Hepatic Cells. *Mol. Biol. Cell*. **20**, 3792–3800 (2009).

29. G. P. Otto, B. J. Nichols, The roles of flotillin microdomains--endocytosis and beyond. *J. Cell Sci.* **124**, 3933–40 (2011).

30. M. Elkabets *et al.*, AXL mediates resistance to PI3Kα inhibition by activating the EGFR/PKC/mTOR axis in head and neck and esophageal squamous cell carcinomas.

Cancer Cell. **27**, 533–546 (2016).

31. A. S. Meyer, M. A. Miller, F. B. Gertler, D. A. Lauffenburger, The Receptor AXL Diversifies EGFR Signaling and Limits the Response to EGFR-Targeted Inhibitors in Triple-Negative Breast Cancer Cells. *Sci Signal*. **6** (2013), doi:10.1126/scisignal.2004155.The.

32. M. K. Nguyen *et al.*, Optogenetic oligomerization of Rab GTPases regulates intracellular membrane trafficking. *Nat. Chem. Biol.* **12**, 431–436 (2016).

33. K. Riento *et al.*, Flotillin proteins recruit sphingosine to membranes and maintain cellular sphingosine-1-phosphate levels. *PLoS One*. **13**, 1–18 (2018).

34. H. Shen *et al.*, Coupling between endocytosis and sphingosine kinase 1 recruitment. *Nat. Cell Biol.* **16**, 652–662 (2014).

35. S. Lima, S. Milstien, S. Spiegel, Sphingosine and sphingosine kinase 1 involvement in endocytic membrane trafficking. *J. Biol. Chem.* **292**, 3074–3088 (2017).

36. T. Kajimoto, T. Okada, S. Miya, L. Zhang, S. Nakamura, Ongoing activation of sphingosine 1-phosphate receptors mediates maturation of exosomal multivesicular endosomes. *Nat. Commun.* **4**, 2712 (2013).

37. N. J. Pyne, A. El, D. R. Adams, S. Pyne, Advances in Biological Regulation Sphingosine 1-phosphate and cancer. *Adv. Biol. Regul.* **68**, 97–106 (2018).

38. D. Siow, B. Wattenberg, The compartmentalization and translocation of the sphingosine kinases: Mechanisms and functions in cell signaling and sphingolipid metabolism. *Crit. Rev. Biochem. Mol. Biol.* **46**, 365–375 (2011).

39. C. Gauthier-rouvière, Flotillin membrane domains in cancer. *Cancer Metastasis Rev.* (2020), doi:10.1007/s10555-020-09873-y.

40. Y. Liu *et al.*, High expression of flotillin-2 is associated with poor clinical survival in cervical carcinoma. **8**, 622–628 (2015).

41. P. A. Gregory *et al.*, An autocrine TGF- /ZEB/miR-200 signaling network regulates establishment and maintenance of epithelial-mesenchymal transition. *Mol. Biol. Cell*. **22**, 1686–1698 (2011).

42. I. Y. Hachim *et al.*, Transforming Growth Factor-beta Regulation of Ephrin Type-A Receptor 4 Signaling in Breast Cancer Cellular Migration. *Sci. Rep.* **7**, 1–15 (2017).

43. K. Pardali, A. Moustakas, Actions of TGF-β as tumor suppressor and pro-metastatic factor in human cancer. *Biochim. Biophys. Acta - Rev. Cancer*. **1775**, 21–62 (2007).

44. M. H. Bailey *et al.*, Comprehensive Characterization of Cancer Driver Genes and Mutations. *Cell*. **173**, 371-385.e18 (2018).

45. D. C. Bessette *et al.*, Using the MCF10A/MCF10CA1a breast cancer progression cell line model to investigate the effect of active, mutant forms of EGFR in breast cancer development and treatment using gefitinib. *PLoS One*. **10**, 1–25 (2015).

46. A. Lu *et al.*, A clathrin-dependent pathway leads to KRas signaling on late endosomes en route to lysosomes. *J. Cell Biol.* **184**, 863–879 (2009).

47. R. Villaseñor, Y. Kalaidzidis, M. Zerial, Signal processing by the endosomal system. *Curr. Opin. Cell Biol.* **39**, 53–60 (2016).

48. M. K. Asiedu *et al.*, AXL induces epithelial-to-mesenchymal transition and regulates the function of breast cancer stem cells. *Oncogene*. **33**, 1316–1324 (2014).

49. W. Leconet *et al.*, Preclinical validation of AXL receptor as a target for antibody-based pancreatic cancer immunotherapy. *Oncogene*. **33**, 5405–5414 (2014).

50. W. Leconet *et al.*, Therapeutic activity of anti-AXL antibody against triple-negative breast cancer patient-derived xenografts and metastasis. *Clin. Cancer Res.* **23**, 2806–2816 (2017).

51. Y. Shen, X. Chen, J. He, D. Liao, X. Zu, Axl inhibitors as novel cancer therapeutic agents. *Life Sci.* **198**, 99–111 (2018).

52. M. A. Goyette *et al.*, The Receptor Tyrosine Kinase AXL Is Required at Multiple Steps of the Metastatic Cascade during HER2-Positive Breast Cancer Progression. *Cell Rep.* **23**, 1476–1490 (2018).

53. M. Schoumacher, M. Burbridge, Key Roles of AXL and MER Receptor Tyrosine Kinases in Resistance to Multiple Anticancer Therapies. *Curr. Oncol. Rep.* **19** (2017), doi:10.1007/s11912-017-0579-4.

54. X. Ye *et al.*, An anti-Axl monoclonal antibody attenuates xenograft tumor growth and enhances the effect of multiple anticancer therapies. *Oncogene*. **29**, 5254–5264 (2010).

55. H. Y. Chew *et al.*, Endocytosis Inhibition in Humans to Improve Responses to ADCC-Mediating Antibodies. *Cell*. **180**, 895-914.e27 (2020).

56. S. R. Joseph *et al.*, An Ex Vivo Human Tumor Assay Shows Distinct Patterns of EGFR Trafficking in Squamous Cell Carcinoma Correlating to Therapeutic Outcomes. *J. Invest. Dermatol.* **139**, 213–223 (2019).

57. C. D. Britten *et al.*, A phase I study of ABC294640, a first-in-class sphingosine kinase-2 inhibitor, in patients with advanced solid tumors. *Clin. Cancer Res.* **23**, 4642–4650 (2017).

58. H. A. Neubauer *et al.*, An oncogenic role for sphingosine kinase 2. *Oncotarget*. **7**, 64886–64899 (2016).

59. N. Nabil, I. Mohamed, T. Okada, T. Kajimoto, S.-I. Nakamura, Essential Role of Sphingosine Kinase 2 in the Regulation of Cargo Contents in the Exosomes from K562 Cells. *Kobe J. Med. Sci*. **63**, 123–129 (2017).

60. D. Hatoum, N. Haddadi, Y. Lin, N. T. Nassif, E. M. McGowan, Mammalian sphingosine kinase (SphK) isoenzymes and isoform expression: Challenges for SphK as an oncotarget. *Oncotarget*. **8**, 36898–36929 (2017).

61. N. C. Hait *et al.*, Role of sphingosine kinase 2 in cell migration toward epidermal growth factor. *J. Biol. Chem.* **280**, 29462–29469 (2005).

62. D. Siow, B. Wattenberg, The compartmentalization and translocation of the sphingosine kinases: Mechanisms and functions in cell signaling and sphingolipid metabolism. *Crit. Rev. Biochem. Mol. Biol.* **46**, 365–375 (2011).

63. M. A. Hanson *et al.*, Crystal Structure of a Lipid G protein-Coupled Receptor. *Science (80-.).* **335**, 851–855 (2012).

64. K. Trajkovic *et al.*, Ceramide triggers budding of exosome vesicles into multivesicular endosomes. *Science (80-.).* **319**, 1244–1247 (2008).

65. T. Kajimoto, T. Okada, S. Miya, L. Zhang, S. I. Nakamura, Ongoing activation of sphingosine 1-phosphate receptors mediates maturation of exosomal multivesicular endosomes. *Nat. Commun.* **4** (2013), doi:10.1038/ncomms3712.

66. M. Fortier *et al.*, RhoE controls myoblast alignment prior fusion through RhoA and ROCK. *Cell Death Differ.* **15**, 1221–1231 (2008).

67. B. H. Sung, T. Ketova, D. Hoshino, A. Zijlstra, A. M. Weaver, Directional cell movement through tissues is controlled by exosome secretion. *Nat. Commun.* **6**, 1–14 (2015).

68. A. Petitjean *et al.*, Properties of the six isoforms of p63: P53-like regulation in response to genotoxic stress and cross talk with δNp73. *Carcinogenesis*. **29**, 273–281 (2008).

69. N. Rohani, A. Parmeggiani, R. Winklbauer, F. Fagotto, Variable Combinations of Specific Ephrin Ligand/Eph Receptor Pairs Control Embryonic Tissue Separation. *PLoS Biol.* **12** (2014), doi:10.1371/journal.pbio.1001955.

70. E. H. Budi, B. P. Muthusamy, R. Derynck, T. Biology, R. Medicine, The insulin response integrates increased TGF-β signaling through Akt-induced enhancement of cell surface delivery of TGF-β receptors. *Sci signal*. **8** (2015), doi:10.1126/scisignal.aaa9432.The.

71. E. Guillaume *et al.*, Flotillin microdomains stabilize cadherins at cell-cell junctions. *J. Cell Sci.* **126** (2013), doi:10.1242/jcs.133975.

72. W. Lehmann *et al.*, ZEB1 turns into a transcriptional activator by interacting with YAP1 in aggressive cancer types. *Nat. Commun.* **7**, 1–15 (2016).

73. H. Xia *et al.*, miR-200a-mediated downregulation of ZEB2 and CTNNB1 differentially inhibits nasopharyngeal carcinoma cell growth, migration and invasion. *Biochem. Biophys. Res. Commun.* **391**, 535–541 (2010).

74. J. Antony *et al.*, The GAS6-AXL signaling network is a mesenchymal (Mes) molecular subtype-specific therapeutic target for ovarian cancer. *Sci. Signal.* **9** (2016), doi:10.1126/scisignal.aaf8175.

75. C. Rossé *et al.*, Control of MT1-MMP transport by atypical PKC during breast-cancer progression. *Proc. Natl. Acad. Sci. U. S. A.* **111**, E1872-9 (2014).

76. V. M. Lakhani SR, Schnitt SJ, Tan PH. *WHO Classif. tumours breast views a Work. Gr. that Conv. a Consens. Editor. Meet. Int. Agency Res. Cancer (IARC), Lyon, Sept. 1-3, 2011. 4. ed.* (2012).

77. H. J. Bloom, W. W. Richardson, Histological grading and prognosis in breast cancer a study of 1409 cases of which 359 have been followed for 15 years. *Br. J. Cancer*. **11**, 359–377 (1957).

78. L. B. Kinsel *et al.*, Immunocytochemical Analysis of Estrogen Receptors as a Predictor of Prognosis in Breast Cancer Patients: Comparison with Quantitative Biochemical Methods. *Cancer Res.* **49**, 1052–1056 (1989).

79. A. C. Wolff *et al.*, American Society of Clinical Oncology/College of American Pathologists guideline recommendations for human epidermal growth factor receptor 2 testing in breast cancer. *J. Clin. Oncol.* **25**, 118–145 (2007).